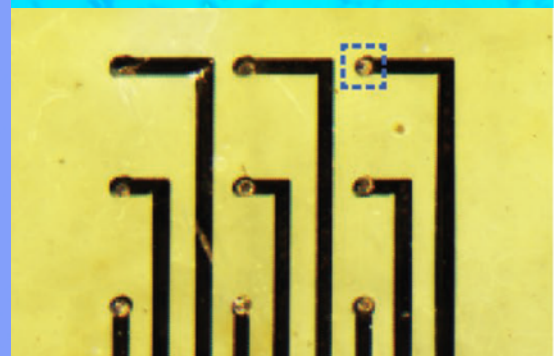
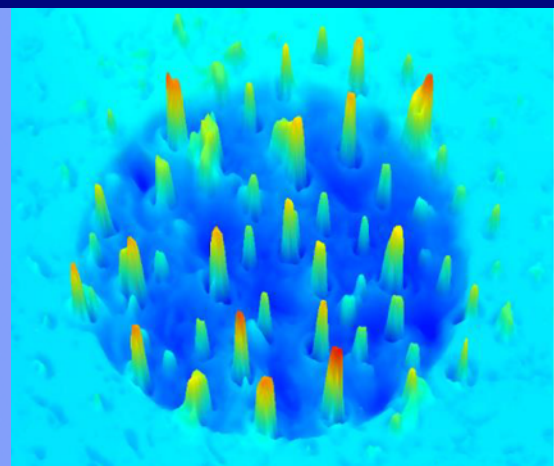
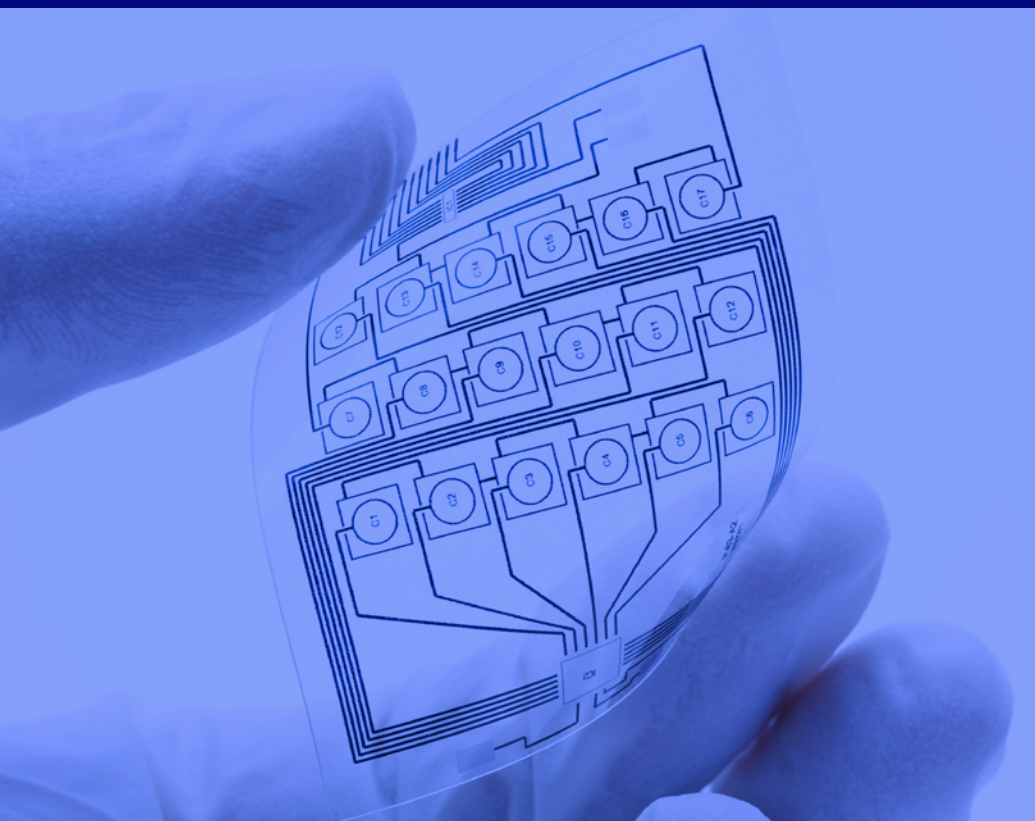


# 03

## Advanced Optical Metrology

### Thin Film Metrology



**OLYMPUS**

**WILEY**

# Contents

- 3** Flexible Thin-Film Electronics  
**Lawrence A. Renna**
- 7** Film Adhesion of Flexible Electronics  
Influenced by Interlayers  
**Andreas Kleinbichler, Mattias Bartosik,  
Bernhard Völker, and Megan J. Cordill**
- 13** Breathable and Flexible Polymer Membranes  
with Mechanoresponsive Electrical Resistance  
**Qiang Gao, Bernd A. F. Kopera, Jian Zhu,  
Xiaojian Liao, Chao Gao, Markus Retsch,  
Seema Agarwal, and Andreas Greiner**
- 20** Super-Resolution Microscopy by Movable  
Thin Films with Embedded Microspheres  
**Kenneth W. Allen, Navid Farahi, Yangcheng Li,  
Nicholaos I. Limberopoulos, Dennis E. Walker Jr.,  
Augustine M. Urbas, Vladimir Liberman,  
and Vasily N. Astratov**
- 27** Flexible Micropillar Electrode Arrays  
for In Vivo Neural Activity Recordings  
**Mingde Du, Shouliang Guan, Lei Gao, Suye Lv, Siting Yang,  
Jidong Shi, Jinfen Wang, Hongbian Li, and Ying Fang**
- 33** Scientific Publishing  
5 tips for writing better science papers
- 36** Scientific Publishing:  
Title and Abstract  
**P. Trevorrow, G. E. Martin**

## Imprint

© Wiley-VCH GmbH  
Boschstr. 12, 69469  
Weinheim, Germany  
Email: [info@wiley-vch.de](mailto:info@wiley-vch.de)  
Editor-in-Chief:  
Dr. Christina Poggel  
Editor: Dr. Lawrence Renna

# Flexible Thin-Film Electronics

Lawrence A. Renna

Alessandro Volta created the first electrical circuit in 1800 using salt-water solutions connected by pieces of metal. Volta went on to invent many electronic systems, most notably the Voltaic Pile (the first battery).<sup>[1]</sup> Fast-forward and electronics are ubiquitous throughout our lives. Most electronic devices are composed of rigid circuit boards containing electronic components (e.g., transistors, resistors, and capacitors), and printed metallic interconnects. Now, flexible electronics are currently being developed for next-generation devices. Flexible electronics can be used for an incomprehensible number of applications,<sup>[2]</sup> but some include, foldable displays, conformal photovoltaics, batteries, power generators, wearable sensors, soft robotics, and bioelectronic interface applications.<sup>[3, 4]</sup>

## 1. FLEXIBLE METALLIC THIN-FILM CONDUCTORS

Flexible electronics require patterned conducting materials that can withstand strain without losing conductivity to enable functionality for a variety of applications. To achieve conducting pathways, or interconnects, different materials can be used including but not limited to conducting polymers (e.g., PEDOT:PSS),<sup>[5, 6]</sup> carbon materials (e.g., graphene, CNTs),<sup>[7, 8]</sup> oxides (e.g., ITO),<sup>[9]</sup> liquid metal (e.g., EGaln),<sup>[10, 11]</sup> metal nanowires,<sup>[12]</sup> and metallic thin films.<sup>[13–16]</sup>

Often, to achieve conducting structures, small islands of rigid electronics are assembled on to a flexible polymer substrate and connected using thin-film metallic interconnects or electrodes. The mechanical properties of the

metal layers and their adhesion to the flexible substrate, especially during strain, are of the utmost importance to their functionality. The failure of these layers is either via i) fracture through the thickness of the layer or ii) the metallic layers delaminate from the substrate.<sup>[16]</sup> Thus the study of metallic interconnects and their failure during strain or bending is imperative to develop flexible electronic devices.

The through-thickness fracture of metallic interconnects can be studied by tensile strain testing and bending experiments. The deformation of metallic thin films on flexible substrates has been examined by tensile testing and monitoring the effects by X-ray diffraction and microscopy.<sup>[17] [18]</sup> For example, Gruber et al. studied the cracking behavior of copper (Cu) films on polyimide (PI) with tantalum (Ta) interlayers. The fracture toughness of the Cu films increases with Cu film thickness and

decreases with increasing Ta interlayer thickness. When the Cu films were thinner than 70 nm, they exhibited inherent brittle fracture.

Furthermore, the mechanical failure of brittle, thin films on a flexible substrate, when bending, can be observed by optical microscopy. Glushko et al. demonstrated the variable mechanical cracking of printed silver (Ag) interconnects via cyclic tensile, compressive, and mixed tensile compressive bending strains. Conversely, evaporated Ag thin films showed no fracture dependence on the type of strain.<sup>[19]</sup>

The adhesion of metallic thin film interconnects to the flexible substrate is also critical to their performance.<sup>[16]</sup> Gold (Au) or Ag are ideal materials for interconnects because they are ductile, have a low electric resistance, and can be easily deposited and patterned. However, these metals sometimes delaminate from flexible polymer substrates. The delamination typically manifests as buckling from the substrate. Therefore, titanium (Ti), tantalum (Ta), or chromium (Cr) interlayers are used to improve the adhesion of metallic thin films to the polymer substrate. Confocal laser scanning microscopy (CLSM) can be used as a tool to measure the buckling of metallic thin films during compression-induced delamination.

As shown in the digest article “Thin Film Adhesion of Flexible Electronics Influenced by Interlayers,” the adhesion properties of Au and Au/Ta thin films on PI, under compressive strain, was investigated.<sup>[16]</sup> CLSM was used to measure the buckling dimensions under compressive strain. The dimensions of the buckles can be used to calculate the critical buckling and driving stresses, using the Hutchinson and Suo model. The studies show that Au thin films spontaneously buckle, while a compressive strain is required to delaminate the Au/Ta film, indicating larger adhesion energy.

#### Further Reading:

<https://onlinelibrary.wiley.com/doi/abs/10.1002/admt.201700277>  
<https://onlinelibrary.wiley.com/doi/10.1002/aenm.201700535>

Appl. Note: [https://www.olympus-ims.com/en/applications/electro-mechanical\\_behavior\\_of\\_thin\\_films/](https://www.olympus-ims.com/en/applications/electro-mechanical_behavior_of_thin_films/)

Appl. Note: [https://www.olympus-ims.com/en/applications/quantitative\\_investigations\\_of\\_the\\_interconnect/](https://www.olympus-ims.com/en/applications/quantitative_investigations_of_the_interconnect/)

## 2. CONDUCTIVE POLYMER MEMBRANES

Flexible electronics can be used for wearable devices for applications such as movement sensors, biological sensors, triboelectric nanogenerators, flexible power supplies, and actuators.<sup>[20]</sup> Obtaining flexible conductors that can withstand high strain and has low resistance is a challenge in the fabrication of flexible electronic devices. Moreover, an additional requirement for wearable electronics, especially those in contact with skin, is that they have relatively high porosity compared to more established flexible electronics. This is because the comfort of wearable devices is contingent on air permeability. Attaining flexibility, elasticity, high conductivity, high mechanical integrity, and porosity is an active research area.<sup>[12]</sup>

Flexible electrodes are generally composed of an elastic substrate as the elastomer to support bending, stretching, and twisting. However, these materials are nonporous and do not provide breathability. One solution to the lack of air permeability of flexible electronics is to prepare conductive polymer membranes. Conductive polymer membranes are composed of a network of stretchable polymer fibers and conductive additives. The network of polymer fibers is inherently porous and allows for gas permeability. Methods of fabrication include the inclusion of conductive additives into yarns, fabrics, and breathable ionic membranes,<sup>[21]</sup> coating of textiles,<sup>[22]</sup> using cellulosic templates, electrospraying,<sup>[22]</sup> electrohydrodynamic direct writing,<sup>[23]</sup> and electrospinning polymer fibers.<sup>[12, 24]</sup>

In the article digest “Breathable and Flexible Polymer Membranes with Mechanoreponsive Electric Resistance,”<sup>[12]</sup> the authors demonstrate a flexible, highly conductive membrane with inherent porosity to allow for gas permeability. The membrane was fabricated by first electrospinning polyurethane (PU) to form polymer nanofiber mats. Conductive Ag nanowires (AgNWs) are dispersed onto a membrane via a filtration method. Finally, a sandwich is made with the AgNW-coated PU membrane and another PU membrane. Polycaprolactone fibers were used to improve the adhesion of the sandwich. The resulting membranes had a low sheet resistance, showed excellent stability to mechanical strain, and allowed gas permeation.

**Further Reading:**

<https://onlinelibrary.wiley.com/doi/abs/10.1002/adma.201908496>

<https://onlinelibrary.wiley.com/doi/10.1002/smll.201703521>

### 3. FLEXIBLE MICROPILLAR ELECTRODE ARRAYS

Flexible electronics have also shown promise in bioelectronic interface applications. Bioelectronic electrodes are essential to investigate the relationship between electricity and biology (electrophysiology).<sup>[25, 26]</sup> Bioelectronic electrodes can be utilized for both bioimpedance and biopotential measurements. Forming intimate interfaces between electrodes and biological matter (e.g., neural tissue) are important to achieve high fidelity biological to electrical signal transduction.<sup>[26]</sup>

For example, neural electrode techniques have considerably improved our ability to understand brain function and have become a tool for the clinical diagnosis and treatment of neurological disorders. Creating tight interfaces, and good electrical contact, between conventional subdural electrodes and neural tissues, is challenging due to their large mechanical mismatch. Thus, flexible electron-

ics are well suited for neural electrode applications. Fabrication of flexible bioelectronics typically uses metal evaporation, atomic layer deposition, photolithography, and transfer printing, and inkjet printing.<sup>[25, 27]</sup> Nonetheless, conventional flexible substrates such as PI and polydimethylsiloxane (PDMS) still have moduli much higher than neural tissue.<sup>[26]</sup>

To address this issue, Du et al. prepared novel flexible micropillar electrode arrays ( $\mu$ PEAs) based on a biotemplate method, which is described in the article digest "Flexible Micropillar Electrode Arrays for In Vivo Neural Activity Recordings."<sup>[26]</sup> The  $\mu$ PEAs were prepared by using a lotus leaf to create a template that was filled with a flexible material and coated in Au for conductivity. Each electrode contained many hierarchical micropillars, which contained surface nano-scale wrinkles (**Figure 1**). The  $\mu$ PEAs were engulfed by the neural tissue, forming a low impedance interface, which allows for *in vivo* multichannel recordings with a high signal-to-noise ratio.

**Further Reading:**

<https://onlinelibrary.wiley.com/doi/full/10.1002/advs.201700625>

<https://onlinelibrary.wiley.com/doi/abs/10.1002/admt.201900566>

<https://onlinelibrary.wiley.com/doi/abs/10.1002/adfm.201503316>

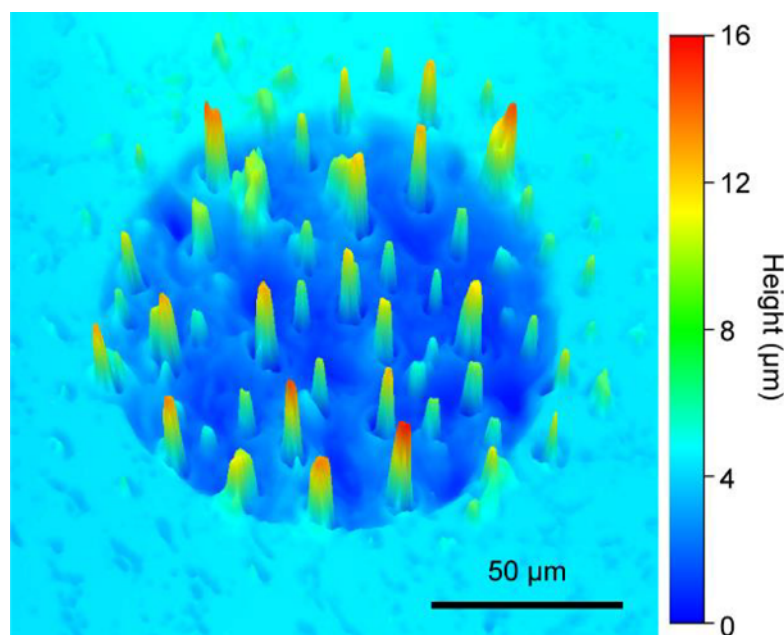


**Figure 1:** 3D confocal image of spatially patterned micropillars on PI substrate.

## REFERENCES

- [1] *A Short History of Circuits and Systems*, in: F. Maloberti, A.C. Davies (Eds.), 2016.
- [2] A. Nathan, A. Ahnood, M.T. Cole, S. Lee, Y. Suzuki, P. Hiralal, F. Bonaccorso, T. Hasan, L. Garcia-Gancedo, A. Dyadyusha, *Flexible electronics: the next ubiquitous platform*, *Proc. IEEE*, 2012, 100 1486–1517.
- [3] S. Huang, Y. Liu, Y. Zhao, Z. Ren, C.F. Guo, *Flexible electronics: stretchable electrodes and their future*, *Adv. Funct. Mater.*, 2019, 29 1805924.
- [4] H. Ling, S. Liu, Z. Zheng, F. Yan, *Organic flexible electronics*, *Small Methods*, 2018, 2 1800070.
- [5] X. Fan, W. Nie, H. Tsai, N. Wang, H. Huang, Y. Cheng, R. Wen, L. Ma, F. Yan, Y. Xia, *PEDOT: PSS for flexible and stretchable electronics: modifications, strategies, and applications*, *Adv. Sci.*, 2019, 6 1900813.
- [6] W. Dang, V. Vinciguerra, L. Lorenzelli, R. Dahiya, *Printable stretchable interconnects*, *Flex. Print. Electron.*, 2017, 2 013003.
- [7] B.K. Sharma, T. Das, J.-H. Ahn, *Graphene for Flexible Electronics*, *Flexible Carbon-based Electronics*, 2018, 95–130.
- [8] Y.Y. Chen, Y. Sun, Q.B. Zhu, B.W. Wang, X. Yan, S. Qiu, Q.W. Li, P.X. Hou, C. Liu, D.M. Sun, *High-Throughput Fabrication of Flexible and Transparent All-Carbon Nanotube Electronics*, *Adv. Sci.*, 2018, 5 1700965.
- [9] V. Zardetto, T.M. Brown, A. Reale, A. Di Carlo, *Substrates for flexible electronics: A practical investigation on the electrical, film flexibility, optical, temperature, and solvent resistance properties*, *J. Polym. Sci. B: Polym. Phys.*, 2011, 49 638–648.
- [10] R. Guo, B. Cui, X. Zhao, M. Duan, X. Sun, R. Zhao, L. Sheng, J. Liu, J. Lu, *Cu–EGaIn enabled stretchable e-skin for interactive electronics and CT assistant localization*, *Mater. Horiz.*, 2020.
- [11] M.g. Kim, C. Kim, H. Alrowais, O. Brand, *Multiscale and Uniform Liquid Metal Thin-Film Patterning Based on Soft Lithography for 3D Heterogeneous Integrated Soft Microsystems: Additive Stamping and Subtractive Reverse Stamping*, *Adv. Mater. Technol.*, 2018, 3 1800061.
- [12] Q. Gao, B.A. Kopera, J. Zhu, X. Liao, C. Gao, M. Retsch, S. Agarwal, A. Greiner, *Breathable and Flexible Polymer Membranes with Mechanoresponsive Electric Resistance*, *Adv. Funct. Mater.*, 2020, 1907555.
- [13] P. Heremans, A.K. Tripathi, A. de Jamblinne de Meux, E.C. Smits, B. Hou, G. Pourtois, G.H. Gelinck, *Mechanical and electronic properties of thin-film transistors on plastic, and their integration in flexible electronic applications*, *Adv. Mater.*, 2016, 28 4266–4282.
- [14] A. Martin, B.S. Chang, Z. Martin, D. Paramanik, C. Frankiewicz, S. Kundu, I.D. Tevis, M. Thuo, *Heat-Free Fabrication of Metallic Interconnects for Flexible/Wearable Devices*, *Adv. Funct. Mater.*, 2019, 29 1903687.
- [15] S.P. Lacour, J. Jones, Z. Suo, S. Wagner, *Design and performance of thin metal film interconnects for skin-like electronic circuits*, *IEEE Electron Device Lett.*, 2004, 25 179–181.
- [16] A. Kleinbichler, M. Bartosik, B. Völker, M.J. Cordill, *Thin Film Adhesion of Flexible Electronics Influenced by Interlayers*, *Adv. Eng. Mater.*, 2017, 19 1600665.
- [17] S. Olliges, P.A. Gruber, V. Auzelyte, Y. Ekinci, H.H. Solak, R. Spolenak, *Tensile strength of gold nanointerconnects without the influence of strain gradients*, *Acta Mater.*, 2007, 55 5201–5210.
- [18] P.A. Gruber, E. Arzt, R. Spolenak, *Brittle-to-ductile transition in ultrathin Ta/Cu film systems*, *J. Mater. Res.*, 2009, 24 1906–1918.
- [19] O. Glushko, M.J. Cordill, A. Klug, E.J. List-Kratochvil, *The effect of bending loading conditions on the reliability of inkjet printed and evaporated silver metallization on polymer substrates*, *Microelectron. Reliab.*, 2016, 56 109–113.
- [20] W. Zeng, L. Shu, Q. Li, S. Chen, F. Wang, X.M. Tao, *Fiber-based wearable electronics: a review of materials, fabrication, devices, and applications*, *Adv Mater*, 2014, 26 5310–5336.
- [21] A. Gugliuzza, E. Drioli, *A review on membrane engineering for innovation in wearable fabrics and protective textiles*, *J. Membr. Sci.*, 2013, 446 350–375.
- [22] Q. Qiu, M. Zhu, Z. Li, K. Qiu, X. Liu, J. Yu, B. Ding, *Highly flexible, breathable, tailorable and washable power generation fabrics for wearable electronics*, *Nano Energy*, 2019, 58 750–758.
- [23] D. Ye, Y. Ding, Y. Duan, J. Su, Z. Yin, Y.A. Huang, *Large-Scale Direct-Writing of Aligned Nanofibers for Flexible Electronics*, *Small*, 2018, 14 1703521.
- [24] C. Wang, K. Xia, H. Wang, X. Liang, Z. Yin, Y. Zhang, *Advanced carbon for flexible and wearable electronics*, *Adv. Mater.*, 2019, 31 1801072.
- [25] Y. Khan, F.J. Pavinatto, M.C. Lin, A. Liao, S.L. Swisher, K. Mann, V. Subramanian, M.M. Maharbiz, A.C. Arias, *Inkjet-printed flexible gold electrode arrays for bioelectronic interfaces*, *Adv. Funct. Mater.*, 2016, 26 1004–1013.
- [26] M. Du, S. Guan, L. Gao, S. Lv, S. Yang, J. Shi, J. Wang, H. Li, Y. Fang, *Flexible Micropillar Electrode Arrays for In Vivo Neural Activity Recordings*, *Small*, 2019, 15 1900582.
- [27] A. Carlson, A.M. Bowen, Y. Huang, R.G. Nuzzo, J.A. Rogers, *Transfer printing techniques for materials assembly and micro/nanodevice fabrication*, *Adv. Mater.*, 2012, 24 5284–5318.

# 01 Film Adhesion of Flexible Electronics Influenced by Interlayers

Andreas Kleinbichler, Mattias Bartosik, Bernhard Völker, and Megan J. Cordill

## ABSTRACT

As flexible electronics emerge for applications such as medical sensors and foldable displays, there is a need to understand the interfacial behavior between the conducting elements and the compliant polymer substrate that the devices are prepared on. Compression-induced delamination is a technique that uses the buckling dimensions to evaluate the interfacial adhesion of materials on flexible substrates quantitatively. This study shows that spontaneous buckles are formed in gold (Au) films, which are deposited without an interlayer. Conversely, external loading is required to delaminate the Au film with the tantalum (Ta) adhesion layer indicating higher adhesion energy.

## INTRODUCTION

Flexible devices and sensors are an emerging field in the electronics sector used for various applications, such as foldable displays<sup>[1,2]</sup> and neural electrodes.<sup>[3,4]</sup> The primary goal in the design of flexible electronics is to achieve significant strain (>10%) without losing electronic functionality. Many designs to achieve this goal consist of small islands of rigid electronics placed on a flexible polymer substrate and connected using metallic lines. In this design, the adhesion between the lines and the underlying substrate is of great importance to device reliability.

The failure of flexible electronic materials occurs via two mechanisms; the fracture of the metallic conducting components through thickness crack formation or the metallic layers delaminate from the substrate. Several testing techniques have been used to analyze cracking failure, the most popular being tensile strain-

ing<sup>[5-9]</sup> and bending.<sup>[10-13]</sup> The techniques used to evaluate the adhesion of thin films to rigid substrates have advanced our understanding of adhesion and its mechanisms.<sup>[14-19]</sup> These methods work well for films on rigid substrates; however, flexible electronics present more challenges, and the methods and models for rigid substrates cannot always be employed. Therefore, tensile-induced delamination<sup>[20,21]</sup> or compression-induced buckling methods<sup>[22,23]</sup> have been developed to this end. These techniques work well for brittle films,<sup>[24-26]</sup> but require an extensive amount of straining for ductile films<sup>[27]</sup> or an overlayer to induce delamination at lower levels of strain.<sup>[28,29]</sup>

Noble metals, such as Au or Ag, are the materials of choice for the connecting lines between the semiconducting islands. It is advantageous to use these metals because they are ductile, have a low electric resistance, and can be easily deposited and patterned. Unfortunately, these metals, sometimes, have trou-

ble adhering to the polymer substrates used in flexible electronics. Therefore, interlayers, like titanium (Ti), tantalum (Ta), and chromium (Cr), are used to improve the adhesion of the noble metal to the polymer substrate.<sup>[26,27,30]</sup> Since the conducting metals used are ductile, methods that can induce defined areas of delamination are desired to determine the effect of interlayers on adhesion energy. Buckling-based techniques are ideal because plastic deformation is minimized, and buckle delamination is well understood.<sup>[31–33]</sup> Spontaneous buckling can occur when the residual stress of the film is large and compressive, typically in the range of 0.5 GPa – 2 GPa, but typically does not occur on polymer substrates because the substrate can accommodate the film stress by macroscopically bending. Conversely, tensile-induced delamination is effective at creating buckles in a ductile film system of 50 nm Cu with a 10 nm Cr interlayer.<sup>[26]</sup>

In this work, compression-induced delamination will be used to cause a 300 nm Au film to buckle upon unloading rather than during loading. Buckling during tensile unloading was compared to spontaneous buckling and used to measure the adhesion energy. With the proper utilization of the different buckling phenomena, the adhesion energy of the interface and how much the addition of interlayers improves adhesion can be quantified.

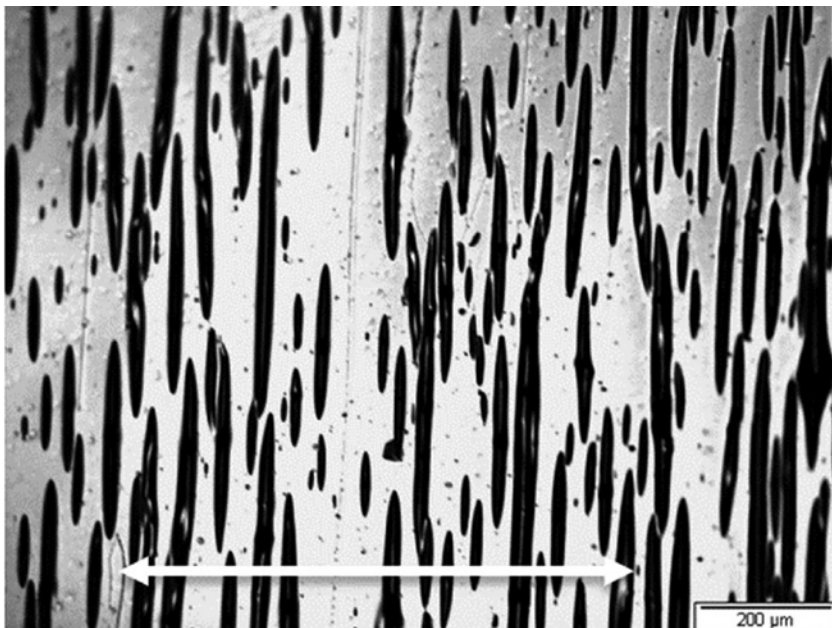


**Figure 1:** Optical micrograph of the Au–Ta film on PI, unloaded after strained to 15%. The straight buckles formed perpendicular to the straining direction (arrow).

## METHODS

Au films (300 nm thick) were sputter-deposited with and without a 10 nm Ta interlayer using a DC Magnetron system onto 50 mm thick Kapton polyimide (PI) substrates.<sup>[3,34]</sup> The Ta film was used as an interlayer to improve the adhesion between Au and PI.

To measure the buckle dimensions, two different devices were used—atomic force microscopy (AFM, Veeco Dimension AFM) and 3D confocal laser-scanning microscopy (CLSM, Olympus® LEXT™ OLS4100 microscope). The CLSM measurements were performed using a laser-wavelength of  $\lambda = 405$  nm. Because its maximum lateral image size is  $80 \mu\text{m} \times 80 \mu\text{m}$  and the vertical limit is 6 mm, the AFM was used only to image smaller buckles. The CLSM can be used to measure all buckle sizes since its vertical limit depends on the distance of the objective to the sample. Gwyddion was used to analyze the images and measure the dimensions of the buckles.<sup>[35]</sup> Additionally, focused ion beam (FIB) cross-sectioning and scanning electron microscopy (SEM) was used to characterize the buckles.

The buckle dimensions are directly related to the critical buckling stress and the delamination stress of the film at the interface. The stresses and the interfacial fracture energies can be calculated using the well-known Hutchinson and Suo model.<sup>[31]</sup> The method is based on the Euler beam theory. The critical buckling stress,  $\sigma_b$ , and the driving stress,  $\sigma_d$ , can be calculated by using **Equations (1) and (2)**.

$$\sigma_b = \frac{\pi^2 E}{12(1-\nu^2)} \left(\frac{h}{b}\right)^2 \quad (1)$$

$$\sigma_d = \sigma_b \left[ \frac{3}{4} \left(\frac{\delta}{h}\right)^2 + 1 \right] \quad (2)$$

where  $\delta$  is the buckling height,  $b$  is the half buckle width,  $h$  is the film thickness,  $E$  is the film's elastic modulus, and  $\nu$  is its Poisson's ratio. The critical buckling stress is the stress necessary to cause film delamination, and the driving stress propagates the buckles. The interfacial fracture energy,  $\Gamma(\psi)$ , for spontaneous buckles is given by **Equation 3** and is used to calculate the adhesion energy of the interfaces.

$$\Gamma(\psi) = \left[ \frac{(1-\nu^2)h}{2E} \right] (\sigma_d - \sigma_b) (\sigma_d - 3\sigma_b) \quad (3)$$

## RESULTS AND DISCUSSION

The Au films on PI (without Ta) delaminated spontaneously at the metal-polymer interface in the form of straight-sided and telephone cord buckles due to the high compressive residual stress in the films, whereas, the Au-Ta films on PI did not delaminate. The typical height and length of the spontaneously formed buckles were on the order of hundreds of nanometers to a few micrometers, respectively.

Therefore, a loading-unloading experiment was performed on the Au-Ta films on PI to create buckles to access the adhesion energy. After straining to a maximum strain of 15% and unloading, straight buckles perpendicular to the straining direction were observed (**Figure 1**). Typically, buckles form parallel to the straining direction when tensile-induced delamination is used because compressive stress builds up due to the difference in the Poisson's ratio between film and substrate.<sup>[20,36]</sup> The

appearance and spacing of the buckles perpendicular to the straining direction are similar to the cracking of brittle films under tension.

To determine the amount of strain required to cause buckling, incremental load-unload testing was. The loading varied between 2% and 14% strain, while the unloading segments always went to 2N. Optical micrographs were taken at the peak strains and every 1% decreasing strain during unloading (**Figure 2a-k**). As shown in **Figure 2a** at 0% strain, no buckles are observed. Upon straining, the film is mostly flat, however small buckles parallel to the straining direction are visible at a preexisting defect in the film. Upon unloading, buckles perpendicular to the straining direction are observed. At lower strains, they are mostly clustered at a series of scratches, but with the increasing strain, the buckles encompass the entire visible area. With each increasing load step, existing interface cracks grow, or more are nucleated which, in

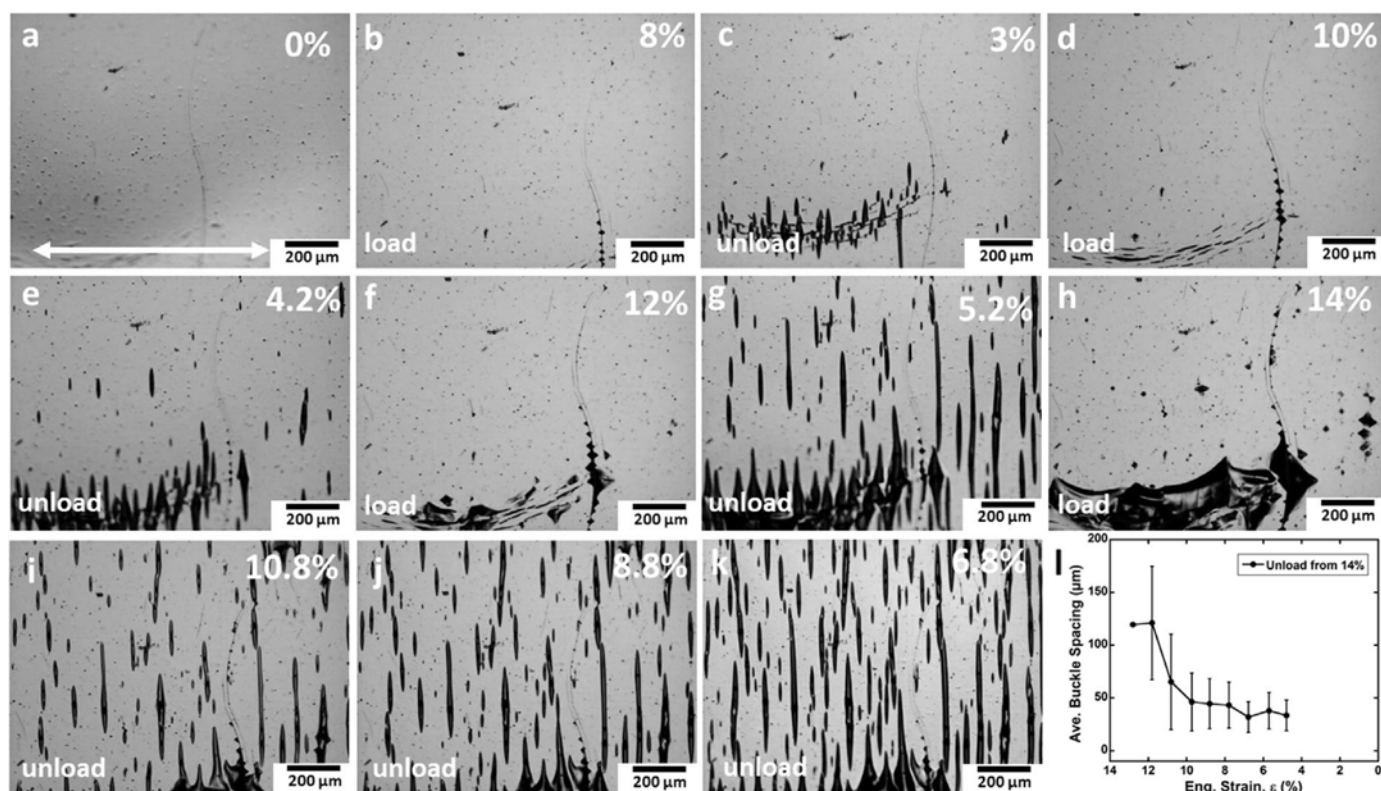


**Figure 2:** In situ optical incremental load-unload experiment. The arrow in (a) indicates the straining direction. In (a), (b), (d), (f), and (h), the film is under tension, in (c), (e), and (g), the film is in an unloaded state, and (i)–(k) is a series during unloading. The buckle spacing decreases with decreasing strain (buckle density increases) and reaches saturation spacing at approximately 7% unloading strain (l). Note that the x-axis in (l) is reversed.

turn, produces more buckles upon unloading. **Figure 2i–k** shows how buckles form and that the density increases during the removal of the tensile load. Finally, **Figure 2l** shows the measured buckle spacing as a function of the unloading from 14% strain. The buckle spacing during unloading follows the same trend as crack spacing during tensile loading, where the spacing decreases until a plateau is reached at approximately 7% unloading strain. Therefore, it was determined that approximately 6% – 8% maximum strain is required to cause delamination upon unloading.

The spontaneous buckle dimensions were measured by AFM (**Figure 3a**) and CLSM (**Figure 3b**) to calculate the adhesion energy of the Au film on PI. **Figure 3b** shows that the delamination starts as single straight-sided buckles and then continues to propagate as telephone cord buckles. This is a common delamination process in biaxially stressed films with spontaneous buckles because of the large shear stress.<sup>[37,38]</sup> The buckles in the white box (**Figure 3b**) are the same as in **Figure 3a**. The same seven single buckles were measured with both imaging methods. CLSM can image a larger area, and it is possible to measure more buckles from a single image. The height of the buckles varies, and the telephone cord buckles are much taller than the single buckles, more than 5  $\mu\text{m}$  in height. Therefore, AFM cannot measure most of the telephone cord buckles due to the maximum deflection limit of the cantilevers. The sample height for the CLSM is only limited to the distance of the objective to the sample, which is a few millimeters. The

marked profiles indicate where the cross-sections have been taken. In **Figure 3c**, the cross-sections of the same buckle measured with the two different methods and shows that the buckle profiles are in good agreement.

Using the elastic properties of  $E_{\text{Au}} = 77$  GPa and the Poisson's ratio  $\nu_{\text{Au}} = 0.44$  of gold, the stresses calculated from the data of both imaging techniques with the Hutchinson and Suo model<sup>[31]</sup> are in good agreement. For example, when AFM measurements are used to calculate the critical buckling stress, the value is  $\sigma_b = 76 \pm 24$  MPa, compared to the CLSM where  $\sigma_b = 74 \pm 23$  MPa is determined. The  $\Gamma(\psi)$  of the spontaneous buckles were calculated from the values measured by AFM and CLSM and are  $\Gamma(\psi) = 0.7 \pm 0.3$  Jm<sup>-2</sup> and  $\Gamma(\psi) = 0.8 \pm 0.3$  Jm<sup>-2</sup>, respectively. The interfacial adhesion values are similar to that for the same interface measured with four-point bending (0.8 Jm<sup>-2</sup>).<sup>[3]</sup>

Because the compression-induced buckles were quite large, only CLSM was used to measure the buckle dimensions (**Figure 4**). The buckle heights are almost three times larger than the spontaneously formed buckles of Au–PI. FIB cross-sectioning was used to determine that the Ta–PI interface fails (**Figure 5**). The critical buckling stress was calculated by **Equation 1** to be approximately 350 MPa. Using **Equations 1 – 3** and the elastic properties of Au, the adhesion energy of the Au–Ta films on PI were determined to be  $\Gamma(\psi) = 11.2 \pm 2.2$  Jm<sup>-2</sup>, which is much higher than the Au film on PI without the Ta interlayer.

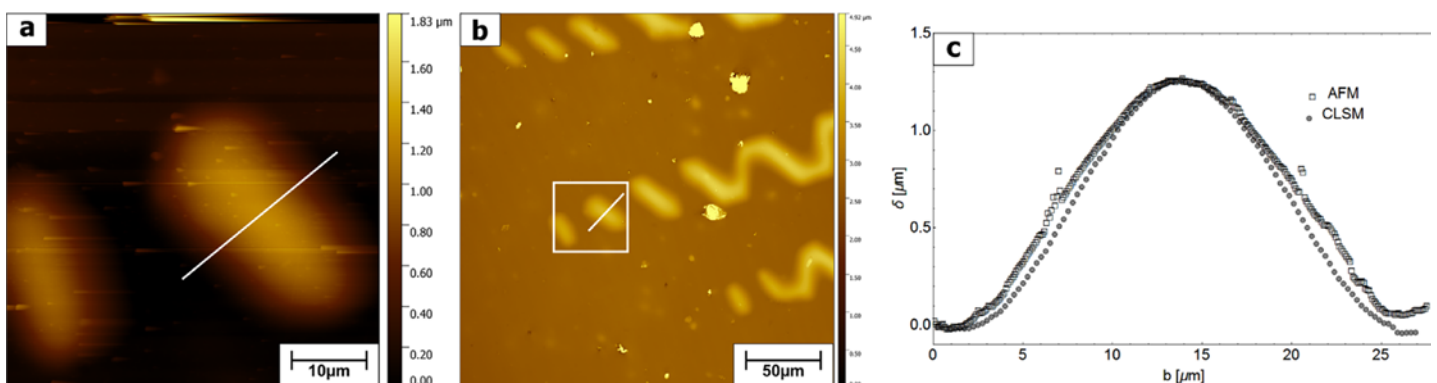


**Figure 3:** (a) AFM height image of the gold film with two spontaneous buckles. (b) CLSM image of an area with the same buckles as in the AFM image. (c) Cross-section of the same buckle taken at approximately the same position

## CONCLUSIONS

In this study, the delamination behavior of the Au–PI film system with and without a Ta interlayer was examined using spontaneously produced buckles and compression-induced buckling. Incremental tensile straining was used to induce buckling of the Au–Ta films on PI. After 6% – 8% applied strain, buckles perpendicular to the straining direction formed during unloading. In situ optical microscopy revealed that after 6% – 8% applied strain, compressive stress significant enough to induce buckling develops due to the elongation of the Au film during straining. The film elongates because the Au film plastically deforms via

uniform necking across the whole film. Necking occurs on account of the good adhesion between the film and substrate, which helps to suppress catastrophic failure. This uniform deformation is in contradiction to the original theory that when a film delaminates from the substrate and becomes freestanding, plastic deformation will localize only at freestanding buckled areas. The Ta interlayer's improved adhesion provides the Au–PI interface, and the formation of the buckles perpendicular to the straining direction were crucial factors necessary to determine how film deformation and delamination are connected. With this new understanding, the lifetime and reliability of flexible electronics can be extended.

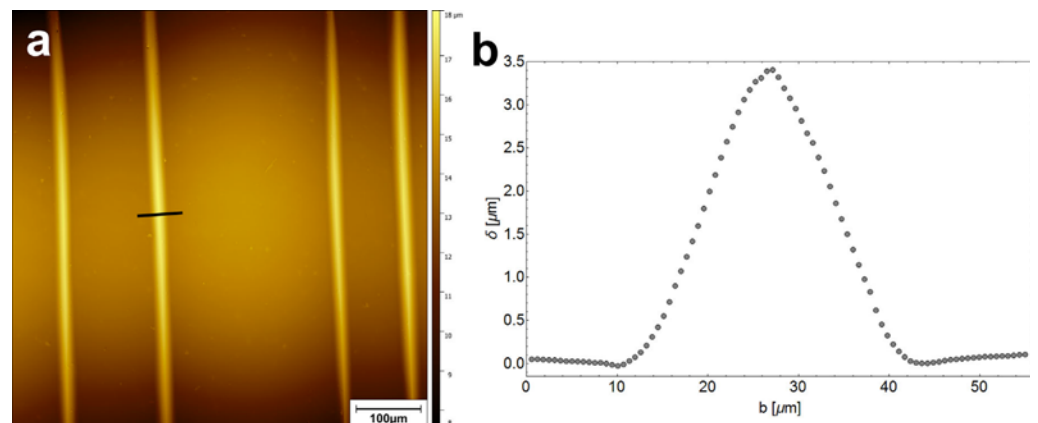


**Figure 4:** (a) CLSM image of an area with the same buckles as in the AFM image. (b) Cross-section of the buckle taken indicated by the black line in (a).

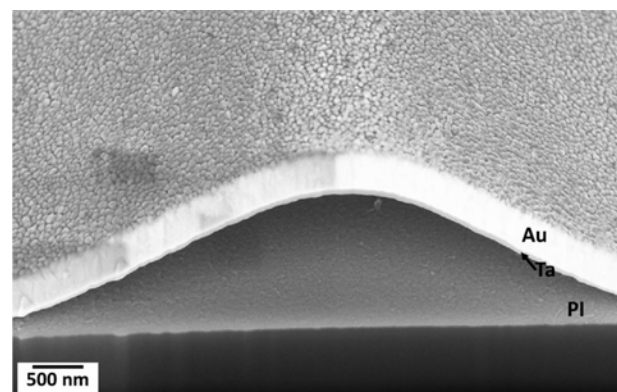


**Figure 5:** FIB cross-section of a buckle indicating that the Ta–PI interface failed as well as demonstrating that localized necking concentrated at the top of the buckle does not occur.

## REFERENCES

- [1] A. C. Siegel, S. T. Phillips, M. D. Dickey, N. Lu, Z. Suo, G. M. Whitesides, *Adv. Funct. Mater.* 2010, 20, 28.
- [2] J. A. Rogers, Z. Bao, K. Baldwin, A. Dodabalapur, B. Crone, V. R. Raju, V. Kuck, H. Katz, K. Amundson, J. Ewing, P. Drzaic, *Proc. Natl. Acad. Sci. U. S. A.* 2001, 98, 4835.
- [3] J. D. Yeager, D. J. Phillips, D. M. Rector, D. F. Bahr, *J. Neurosci. Methods* 2008, 173, 279.
- [4] B. A. Hollenberg, C. D. Richards, R. Richards, D. F. Bahr, D. M. Rector, *J. Neurosci. Methods* 2006, 153, 147.
- [5] D. C. Agrawal, R. Raj, *Acta Metall.* 1989, 37, 1265.
- [6] G. Rochat, Y. Leterrier, P. Fayet, J. Manson, *Thin Solid Films* 2003, 437, 204.
- [7] S. Olliges, P. A. Gruber, V. Auzelyte, Y. Ekinci, H. H. Solak, R. Spolenak, *Acta Mater.* 2007, 55, 5201.
- [8] P. A. Gruber, E. Arzt, R. Spolenak, *J. Mater. Res.* 2009, 24, 1906.
- [9] O. Glushko, M. J. Cordill, *Exp. Tech.* 2014, 40, 303.
- [10] W. P. Vellinga, J. T. M. de Hosson, P. C. P. Bouten, *J. Appl. Phys.* 2011, 110, 7.
- [11] Q. Guan, J. Laven, P. C. P. Bouten, G. de With, *Thin Solid Films* 2016, 611, 107.
- [12] O. Glushko, M. J. Cordill, A. Klug, E. J. W. List-Kratochvil, *Microelectron. Reliab.* 2016, 56, 109.
- [13] G. D. Sim, Y. Hwangbo, H. H. Kim, S. B. Lee, J. J. Vlassak, *Scr. Mater.* 2012, 66, 915.
- [14] K. L. Mittal, *Electrocompon. Sci. Technol.* 1976, 3, 21.
- [15] A. A. Volinsky, N. R. Moody, W. W. Gerberich, *Acta Mater.* 2002, 50, 441.
- [16] M. Lane, R. H. Dauskardt, A. Vainchtein, H. Gao, *J. Mater. Res.* 2000, 15, 2758.
- [17] D. B. Marshall, A. G. Evans, *J. Appl. Phys.* 1984, 56, 2632.
- [18] A. Bagchi, A. G. Evans, *Thin Solid Films* 1996, 286, 203.
- [19] M. J. Cordill, D. F. Bahr, N. R. Moody, W. W. Gerberich, *IEEE Trans. Device Mater. Reliab.* 2004, 4, 163.
- [20] M. J. Cordill, F. D. Fischer, F. G. Rammerstorfer, G. Dehm, *Acta Mater.* 2010, 58, 5520.
- [21] J. Andersons, S. Tarasovs, Y. Leterrier, *Thin Solid Films* 2009, 517, 2007.
- [22] G. Parry, C. Coupeau, J. Colin, A. Cimetière, J. Grilhé, *Acta Mater.* 2004, 52, 3959.
- [23] G. Parry, J. Colin, C. Coupeau, F. Foucher, A. Cimetière, J. Grilhé, *Acta Mater.* 2005, 53, 441.
- [24] M. J. Cordill, A. A. Taylor, *Thin Solid Films* 2015, 589, 209.
- [25] A. A. Taylor, M. J. Cordill, L. Bowles, J. Schalko, G. Dehm, *Thin Solid Films* 2013, 531, 354.
- [26] V. M. Marx, C. Kirchlechner, I. Zizak, M. J. Cordill, G. Dehm, *Philos. Mag.* 2015, 95, 1982.
- [27] B. Putz, R. L. Schoeppner, O. Glushko, D. F. Bahr, M. J. Cordill, *Scr. Mater.* 2015, 102, 23.
- [28] M. J. Cordill, V. M. Marx, C. Kirchlechner, *Thin Solid Films* 2014, 571, 302.
- [29] M. J. Cordill, O. Glushko, B. Putz, *Front. Mater.* 2016, 3, 1.
- [30] S. Frank, U. A. Handge, S. Olliges, R. Spolenak, *Acta Mater.* 2009, 57, 1442.
- [31] J. W. Hutchinson, Z. Suo, *Adv. Appl. Mech.* 1992, 29, 63.
- [32] F. Cleymand, C. Coupeau, J. Colin, J. Grilhé, *Eur. Phys. J. Appl. Phys.* 2000, 10, 3.
- [33] P. O. Renault, P. Villain, C. Coupeau, P. Goudeau, K. F. Badawi, *Thin Solid Films* 2003, 424, 267.
- [34] J. D. Yeager, D. F. Bahr, *Thin Solid Films* 2010, 518, 5896.
- [35] D. Nečas, P. Klapetek, *Open Phys.* 2012, 10, 181.
- [36] F. Toth, F. G. Rammerstorfer, M. J. Cordill, F. D. Fischer, *Acta Mater.* 2013, 61, 2425.
- [37] M. J. Cordill, D. F. Bahr, N. R. Moody, W. W. Gerberich, *Mater. Sci. Eng. A* 2007, 443, 150.
- [38] J.-Y. Faou, G. Parry, S. Grachev, E. Barthel, *Phys. Rev. Lett.* 2012, 108, 1.

# 02 Breathable and Flexible Polymer Membranes with Mechano-responsive Electrical Resistance

Qiang Gao, Bernd A. F. Kopera, Jian Zhu, Xiaojian Liao, Chao Gao, Markus Retsch, Seema Agarwal, and Andreas Greiner

## ABSTRACT

Flexible low-resistance membranes that tolerate very high deformability, produce low joule heating, and allow the passage of gases for human comfort are desired for wearable devices. Herein, a network of silver nanowires (AgNWs) between two highly porous electrospun thermoplastic polyurethane (TPU) membranes is presented. The membranes are mechanically robust (both for bending and stretching) and can withstand large strain before breakage ( $> 700\%$ ). The sheet resistance is as low as  $< 0.1 \Omega \text{ sq}^{-1}$ , and only increases to  $1.6 \Omega \text{ sq}^{-1}$  upon stretching to 100% strain. The combination of polymer elasticity and the AgNW network structure provides a reversible change in resistance beyond 100% strain. This flexible, sandwich-like, electrically conductive membrane is a promising candidate for smart wearable devices and soft robotics.

## INTRODUCTION

Traditional electronics are typically composed of intrinsically heavy and rigid materials, like silicon, metals, and glass, which have minimal flexibility, stretchability, bendability, twistability, and impact resistance. There is a need for flexible and deformable circuits and electrodes with low electric resistance that maintain performance even in a strained state for lightweight, wearable, and flexible electronic devices. <sup>[1–3]</sup> Efforts to construct flexible circuits and electrodes with low resistance focused on elastomeric electrically conductive materials. <sup>[4–10]</sup> These materials are promising for a variety of applications; <sup>[11–17]</sup> however, obtaining

flexible conductors with both high strain properties and low resistance is still a challenge. <sup>[18]</sup> Further, porosity is an essential requirement for the comfort of wearable electronic devices that contact skin to allow air for permeability.

Presently, flexible electrodes are composed of an elastic substrate, such as polydimethylsiloxane (PDMS), <sup>[19–20]</sup> thermoplastic polyurethane (TPU), <sup>[21]</sup> and electrically conductive materials. <sup>[22–26]</sup> Low-resistance electrodes provide the advantages of less energy loss and reduced joule heating. Silver is an excellent material for electrodes and is often used for flexible electrodes with low resistance. <sup>[27]</sup> In our previous work, we prepared electrospun polymer membranes with a metal-like conduc-

tivity of  $7.5 \times 10^5 \text{ S m}^{-1}$  using a very low content (3.35 vol. %) of silver nanowires (AgNWs).<sup>[6]</sup> However, this kind of electrically conductive membrane is bendable but not sufficiently stretchable and is inherently nonporous.

Electrospinning is a promising technique for fabricating porous substrates with high conductivity, flexibility, and air permeability. The ability to electrospin many different polymer types also provides the advantage of tuning the membrane's mechanical characteristics. For example, electrospun polyamide nanofiber nonwovens embedded with AgNW networks showed 50% stretchability and a sheet resistance of  $8.2 \text{ } \Omega \text{ sq}^{-1}$ .<sup>[28]</sup> Electrospun polyurethane nonwoven porous substrate coated with AgNW provided a highly stretchable membrane (more than 300%) with high conductivity.<sup>[29]</sup>

Herein, we present a flexible and breathable polymer membrane with bending and stretching stability and very low electrical resistance. We also provide important fundamental studies on island formation, anisotropy, hot spots, and thermal transport in such structures. We present a simple and scalable preparation method for making such membranes. We use a network of AgNWs as con-

ductive layer sandwiched between two porous electrospun TPU nanofibrous networks. We improved the interface stability with short polycaprolactone (PCL) fibers dispersed in between the AgNWs. Our membranes show a sheet resistance as low as  $<0.1 \text{ } \Omega \text{ sq}^{-1}$ . The resistance does not significantly increase upon deformation (twisting, bending, and stretching to approximately 100% strain). We also show a reversible change in the resistance upon stretching or bending with more than 100% strain for several cycles. The AgNW networks reversibly break and reform during stretching and releasing, respectively. These membranes are breathable, which allows the exchange of gases. Lastly, the membranes have a lower thermal conductivity compared to other porous polymers, despite their electrical conductivity. These membranes are a promising material for electrodes in smart textiles and other wearable devices.

## METHODS

The concept for the preparation of flexible and breathable electrically conductive membranes is illustrated in **Figure 1**. First, we prepared TPU nanofiber nonwovens via elec-

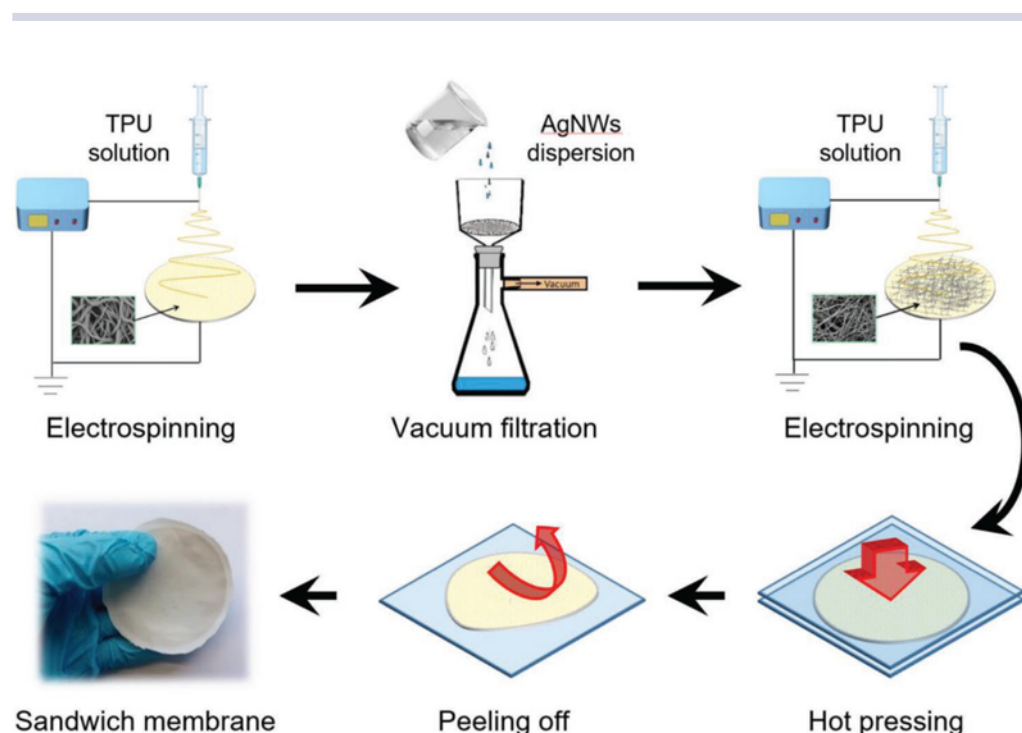


**Figure 1:** Schematic of preparing the TPU-AgNW/PCL-TPU membrane by sandwiching a network of AgNWs between TPU layers.

trospinning. We then used the porous TPU membranes as a filter for the filtration of AgNWs ( $17 \text{ mg mL}^{-1}$ ,  $126 \pm 10 \text{ nm}$  in diameter, and  $18 \pm 4 \mu\text{m}$  in length) mixed with a PCL short-fiber dispersion ( $1 \text{ mg mL}^{-1}$ , average aspect ratio  $\approx 1000$ ). Another layer of TPU nanofibers was electrospun on top of the AgNWs and PCL short fibers. To induce thermal annealing, the achieved sandwich-like, electrically conductive nonwovens were pressed between two glass plates and heated at a temperature of  $75 \text{ }^\circ\text{C}$  ( $167 \text{ }^\circ\text{F}$ ) for 30 minutes to melt the PCL fibers and bond the two layers of TPU nonwovens and AgNWs together.

A Zeiss LEO 1530 was used for scanning electron microscopy (SEM) characterization of the AgNWs and their corresponding networks. Energy dispersive X-ray analysis (EDX) was performed using a Zeiss Ultra Plus ( $V = 10 \text{ kV}$ ). Optical microscopy was performed

using an Olympus® LEXT™ OLS5000 confocal laser scanning microscope. A  $100\times$  magnification lens with a working distance of  $300 \mu\text{m}$  was used. Image analysis was conducted with Matlab.<sup>[30]</sup> The gas permeability test was performed with a homemade unit.<sup>[5]</sup> Tensile tests were carried out using a tensile tester (ZwickiLine Z0.5; BT1-FR0.5TN. D14). Sheet resistance measurements (four-point measurements) were performed using a Keithley 2420 high-current source meter coupled with a Signatone SYS-301. A digital multimeter (EMOS Multimeter EM391) connected to measure the sample with a bronze conductor was employed to measure the stretching resistance and bending resistance. Thermography imaging was performed with an Infracore VarioCAM HD research IR camera. Thermal diffusivity was measured with our own, self-built Lock-In thermography setup.<sup>[31-32]</sup>

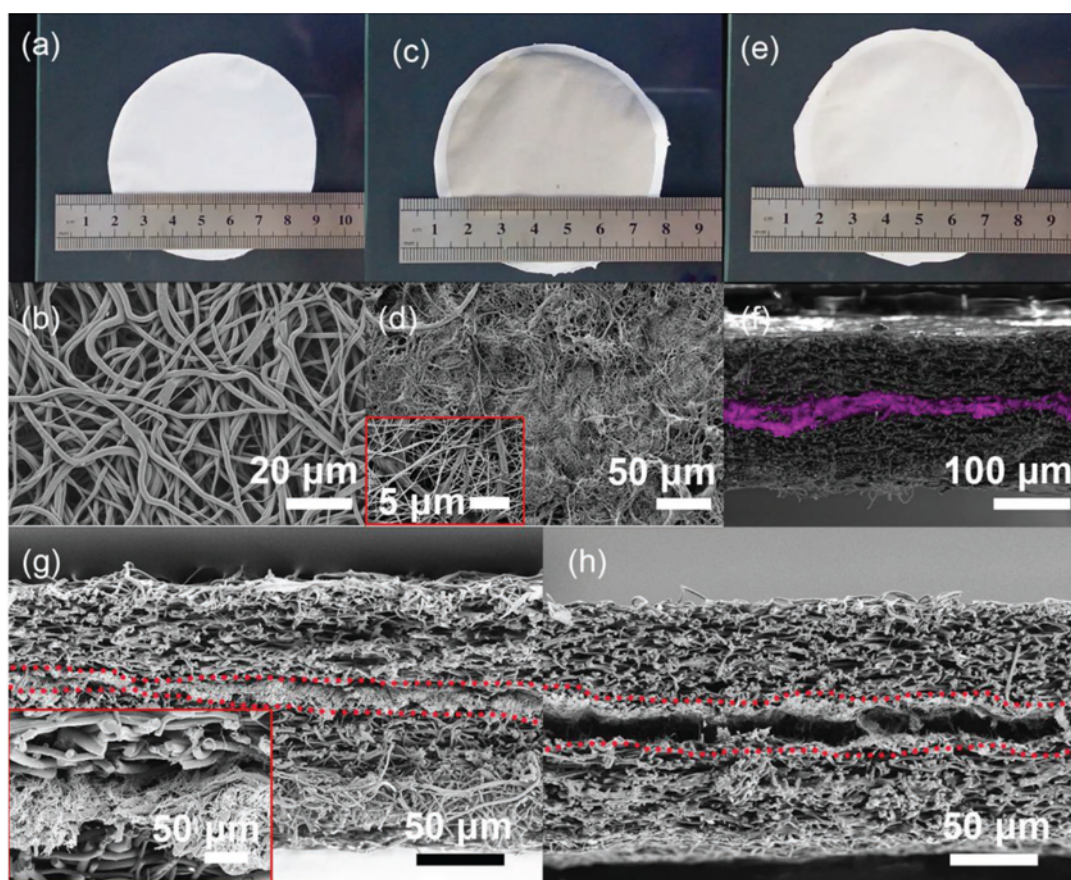


**Figure 2:** a,c) Photograph and b,d) SEM image of the electrospun TPU nonwoven and TPU with AgNWs and PCL, respectively. e) Photograph of TPU-AgNW/PCL-TPU. f) Cross-section of EDX overlaid SEM image of TPU-AgNW/PCL-TPU. g) Cross-section SEM of TPU-AgNW/PCL-TPU and h) TPU-AgNW-TPU.

## RESULTS AND DISCUSSION

The TPU nonwovens consist of randomly oriented fibers (the 2D order parameter is around 0.1) with an average diameter of  $1.6 \pm 0.5 \mu\text{m}$  (**Figure 2a,b**). After filtration, the AgNWs and short PCL fibers generated a double network-type structure due to percolation (**Figure 2c,d**). Afterward, we covered the AgNW/PCL layer with another layer of TPU nonwoven by electrospinning. Finally, we hot pressed the three-layer stack at  $75^\circ\text{C}$  ( $167^\circ\text{F}$ ) for 30 minutes to melt the PCL and increase the adhesion of the layers (**Figure 2e**).

The resulting three-layer membranes are designated as TPU-AgNW/PCL-TPU. We checked the presence of an AgNW layer sandwiched between the two TPU layers with PCL short fibers by EDX (**Figure 2f**). The cross-sectional SEM images of TPU-AgNW/PCL-TPU and TPU-AgNW-TPU (without the use of PCL short fibers for comparison) are shown in **Figure 2g,h**, respectively. The PCL short-fiber dispersion acts as a glue between the AgNW network and the TPU. The TPU-AgNW/PCL-TPU membranes also possess good gas ( $\text{CO}_2$ ) permeability.

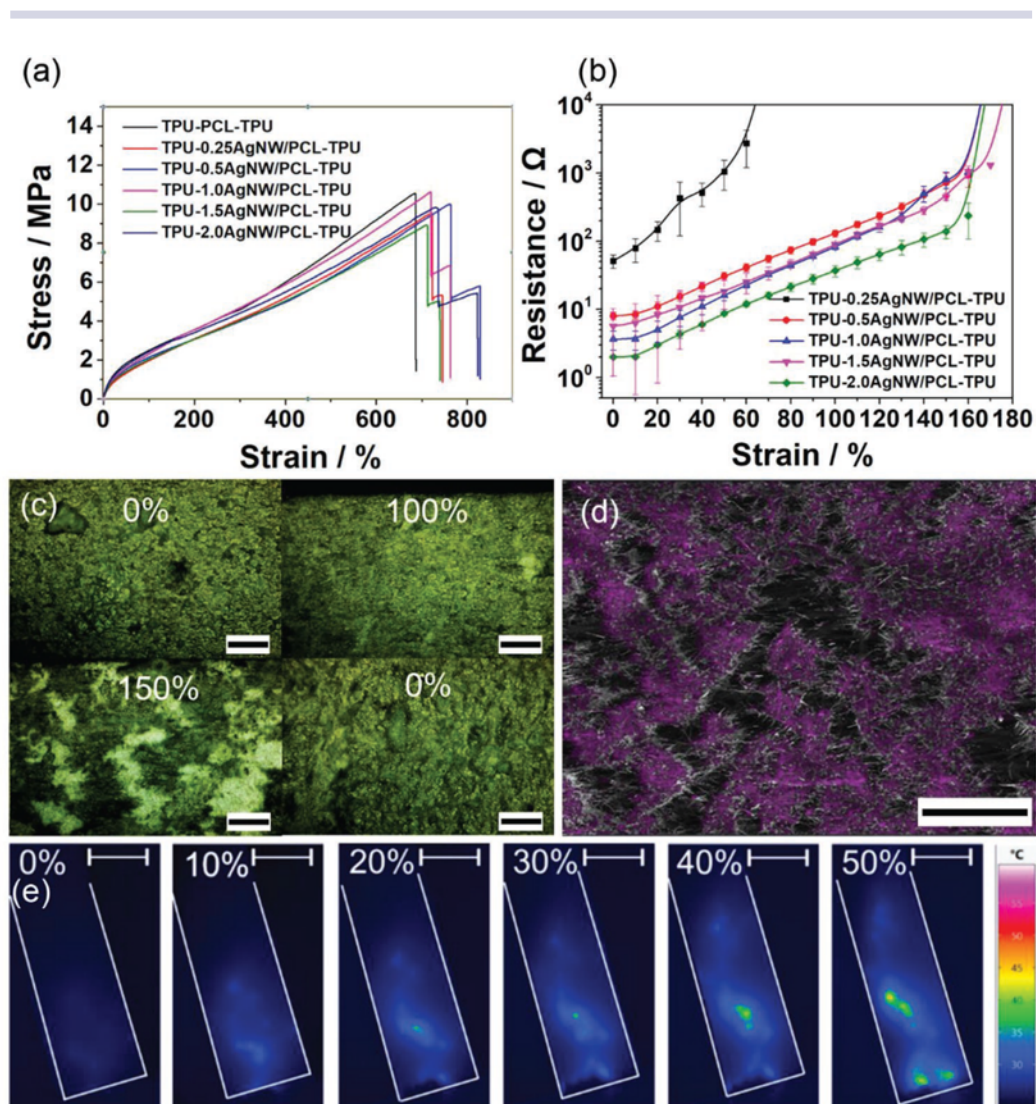


**Figure 3:** a) Stress–strain curves of sandwich membranes with different amounts of AgNWs. b) Resistance of membranes with different amounts of AgNWs with different strains. c) Optical microscopy images of TPU-2.0AgNW/PCL under different stains. (scale bar: 500  $\mu\text{m}$ ) d) EDX-SEM image of TPU-2.0AgNW/PCL at 100% strain. (scale bar: 50  $\mu\text{m}$ ) Ag is indicated in purple. e) Thermography images upon stretching (scale bars: 3 mm).

Different amounts of the AgNW dispersion were used to investigate the influence of the AgNW concentration on the air permeability and electrical properties. The sheet resistance was  $6.1 \pm 0.3 \times 10^8 \Omega \text{ sq}^{-1}$  without an AgNW layer. The sheet resistance decreased to  $0.09 \Omega \text{ sq}^{-1}$  with 8.5 wt.% AgNWs. Even the use of a small amount of AgNWs (1.2 wt.%) significantly decreased the resistance to  $\approx 1 \Omega \text{ sq}^{-1}$ . Further reduction in the amount of AgNW to  $\approx 0.5$  wt% led to a sharp increase in the sheet resistance ( $2.4 \pm 3.1 \times 10^6 \Omega \text{ sq}^{-1}$ ). This result indicates that the percolation threshold of AgNW is 0.5 wt.% – 1.2 wt.%.

The sandwich membranes exhibited a breaking stress of  $\approx 8$  MPa. The TPU without AgNWs had breaking stress of  $\approx 10$  MPa. The membranes with different amounts of AgNWs can be stretched to over 700% (**Figure 3a**). The membranes showed 10% and 30% creep after stretching for 100 cycles to 50% and 100% strain, respectively. We measured the resistance as a function of % strain (**Figure 3b**). TPU-AgNW/PCL-TPU can tolerate considerable strains with a moderate increase in resistance depending upon the amount of AgNWs. The sample with the highest content of AgNWs (8.5 wt.%) changed its resistance by only two orders of magnitude at a strain of  $\approx 150\%$ . In contrast, the sample with the fewest AgNWs (1.2 wt.%) showed a comparable increase in resistance already at a strain of only 60%.

**Figure 3c** shows the optical microscopy images of the AgNW layer after 0%, 100%, and 150% stretching and recovering to 0% again for the sample with 8.5 wt% AgNWs. When the membrane was stretched up to 100%, few cracks could be observed in the AgNW layer. However, upon further stretching to approximately 150%, large cracks (bright area), in an island-like fashion, were observed, causing a significant increase in resistance. The formation of island-like structures is confirmed by EDX measurement (**Figure 3d**). The separated islands and cracks restricted the flow of electricity and created hot spots due to joule heating at the bottlenecks. Such hotspots can be imaged by infrared thermography when applying a DC current (**Figure 3e**).

We employed direction-dependent lock-in thermography to gain a better insight into the composite morphology. Using a line laser as a heat source, we can probe the overall thermal diffusivity in such a composite sample along different orientations relative to the stretching direction. We see in **Figure 4a–c** that the TPU

fibers align parallel to the stretching direction. Image analysis of these laser scanning microscopy images reveals that the fiber orientation is already complete at a strain of  $\approx 100\%$ .

The 2D order parameter ( $S_{2D}$ ) measures how well the fibers are aligned. The order parameter is given by **Equation 1**.

$$S_{2D} = \frac{2}{N} [\sum_{i=1}^N (\cos(\alpha_i - \bar{\alpha}))^2]^{-1} \quad (1)$$

where  $N$  is the number of stretched fiber orientations in the SEM image,  $\alpha_i$  is the angle between the  $i^{\text{th}}$  fiber and the horizontal axis, and  $\bar{\alpha}$  is the average angle.<sup>[30]</sup> The  $S_{2D}$  of pure TPU remains constant at a value close to 1.0 after 100% strain (**Figure 4d**). For pure TPU, the thermal diffusivity increases along the stretching direction and decreases perpendicular to it (**Figure 4e,f**). Since TPU is a thermal insulator, the absolute thermal diffusivity remains at a low level. Heat travels along these oriented fibers faster than perpendicular to it, resulting in a high anisotropy ratio (**Figure 4g**). For AgNW-TPU, some degree of anisotropy evolves (**Figure 4h,i**), but the overall thermal diffusivity decreases compared to the unstretched state. Simultaneously, for AgNW-TPU samples, we find an evolution of anisotropic heat spreading (**Figure 4g**). Overall, the stretching of the AgNW-TPU sample leads to a smaller amount of anisotropy compared to the pure TPU network structure (**Figure 4g**).

The membranes showed excellent stretchability and bending stability. The samples were subjected to 100 cycles of stretching and bending. The resistance change (RC) can be described by **Equation 2**:

$$RC = \frac{R}{R_0} \quad (2)$$

where  $R$  is the time-dependent resistance and  $R_0$  is the initial resistance measured after stretching and bending tests. The RC of the sample with 1.2 wt% of AgNWs significantly increased after only 60 stretching cycles; the RC was  $>20\,000$  under 50% strain. However, the same sample showed much better bending stability (bending curvature from  $0^\circ$  to  $150^\circ$ ) without a significant change in resistance. The RC of TPU-0.25AgNW/PCL-TPU after 100 bending cycles was merely 1.32. The sample TPU-2.0AgNW/PCLTPU with a dense network of AgNWs showed both excellent bending and stretching stability. No significant change in the RC was observed for bending tests. During strain testing, RC increased by only a factor of  $\approx 20$  after 100 cycles.

## CONCLUSIONS

In conclusion, we have demonstrated a new strategy to fabricate sandwich-like electrically conductive membranes with very low electric resistance. Our material consists of an AgNW network sandwiched between two porous electrospun TPU nonwovens. PCL short fibers act as glue and provide a robust inter-

face between the three layers. Our membranes show excellent bending and stretching stability, high stretchability, and very low initial electric resistance ( $<0.1 \Omega \text{ sq}^{-1}$ ). Additionally, the membrane possesses gas permeability and low thermal diffusivity. Furthermore, the material has the potential to be integrated into smart wearable devices.

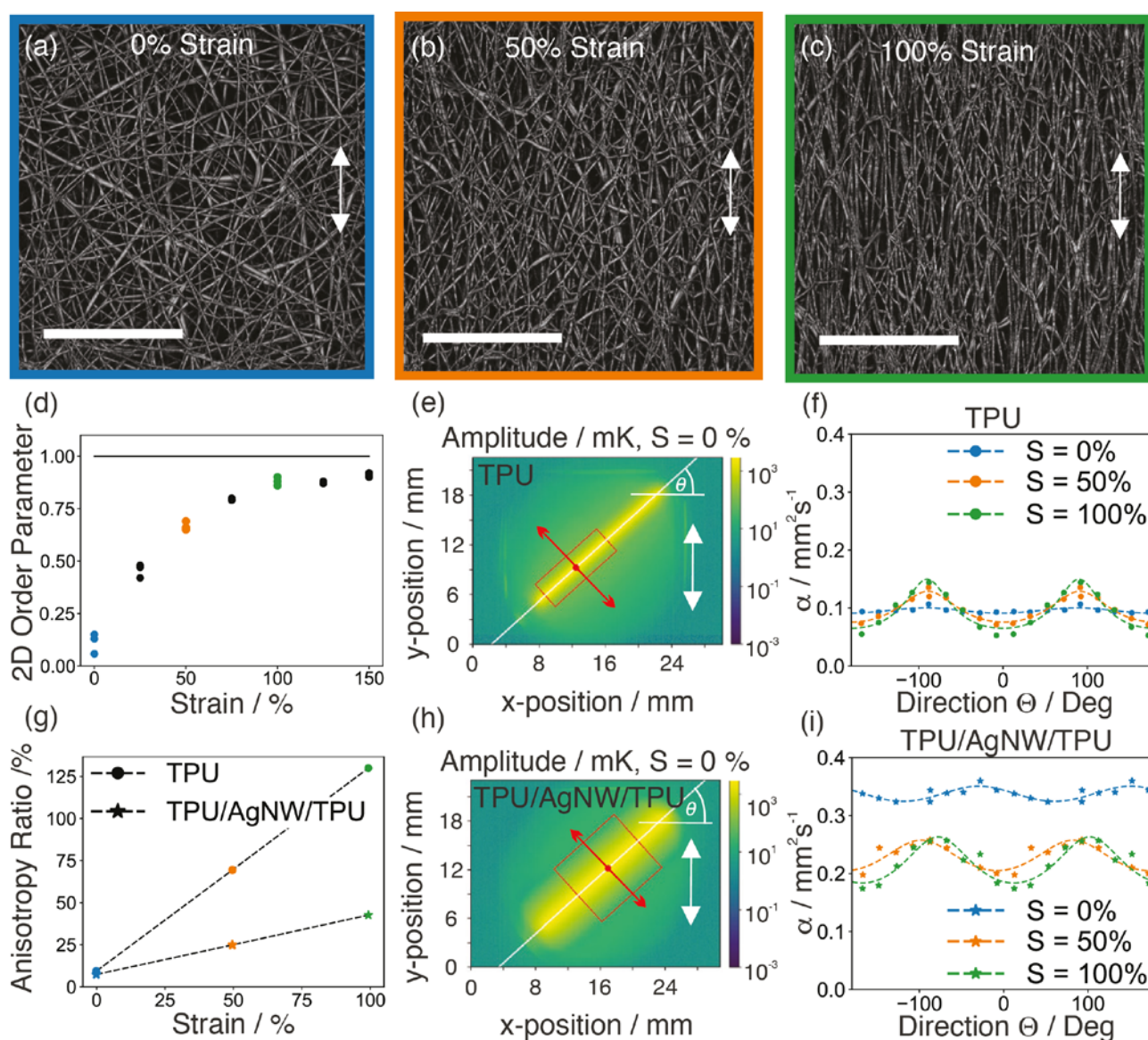


**Figure 4:** a–c) Laser scanning microscopy images of TPU fibers (scale bars: 50  $\mu\text{m}$ ). The fibers align in the stretching direction (white arrows) with increasing strain,  $S$ . d) The 2D order parameter for the fiber orientation derived from laser scanning microscopy images with increasing strain. e) Temperature amplitude as a function of position on the surface of a pure TPU. f) Thermal diffusivity as a function of direction ( $0^\circ$  is horizontal) and strain for a pure TPU (f). Anisotropy ratios for the thermal diffusivity. g) The pure TPU shows a stronger anisotropy than the TPU-2.0AgNW/PCL-TPU. h) Temperature amplitude as a function of position on the surface of TPU-2.0AgNW/PCL-TPU film with 0% strain. i) Thermal diffusivity as a function of direction ( $0^\circ$  is horizontal) and strain for TPU-2.0AgNW/PCL-TPU film.

## REFERENCES

- [1] E. J. Markvicka, M. D. Bartlett, X. N. Huang, C. Majidi, *Nat. Mater.* 2018, 17, 618.
- [2] Y. J. Hong, H. Jeong, K. W. Cho, N. Lu, D. H. Kim, *Adv. Funct. Mater.* 2019, 29, 1808247.
- [3] S. Y. Huang, Y. Liu, Y. Zhao, Z. F. Ren, C. F. Guo, *Adv. Funct. Mater.* 2019, 29, 1805924.
- [4] S. H. Jiang, S. Reich, B. Uch, P. Hu, S. Agarwal, A. Greiner, *ACS Appl. Mater. Interfaces* 2017, 9, 34286.
- [5] Y. Zhou, C. J. Wan, Y. S. Yang, H. Yang, S. C. Wang, Z. D. Dai, K. J. Ji, H. Jiang, X. D. Chen, Y. Long, *Adv. Funct. Mater.* 2019, 29, 1806220.
- [6] S. Reich, M. Burgard, M. Langner, S. Jiang, X. Wang, S. Agarwal, B. Ding, J. Yu, A. Greiner, *npj Flexible Electron.* 2018, 2, 5.
- [7] Y. Q. Zeng, T. Li, Y. G. Yao, T. Y. Li, L. B. Hu, A. Marconnet, *Adv. Funct. Mater.* 2019, 29, 1901388.
- [8] W. Weng, P. N. Chen, S. S. He, X. M. Sun, H. S. Peng, *Angew. Chem., Int. Ed.* 2016, 55, 6140.
- [9] S. Lee, S. Shin, S. Lee, J. Seo, J. Lee, S. Son, H. J. Cho, H. Algadi, S. Al-Sayari, D. E. Kim, T. Lee, *Adv. Funct. Mater.* 2015, 25, 3114.
- [10] J. Lee, B. L. Zambrano, J. Woo, K. Yoon, T. Lee, *Adv. Mater.* 2019, 1902532.
- [11] R. Cao, X. J. Pu, X. Y. Du, W. Yang, J. N. Wang, H. Y. Guo, S. Y. Zhao, Z. Q. Yuan, C. Zhang, C. J. Li, Z. L. Wang, *ACS Nano* 2018, 12, 5190.
- [12] M. Amjadi, M. Sitti, *Adv. Sci.* 2018, 5, 1800239.
- [13] R. P. Tong, G. X. Chen, D. H. Pan, H. S. Qi, R. A. Li, J. F. Tian, F. C. Lu, M. H. He, *Bio-macromolecules* 2019, 20, 2096.
- [14] A. Chortos, J. Liu, Z. Bao, *Nat. Mater.* 2016, 15, 937.
- [15] S. H. Wang, J. Y. Oh, J. Xu, H. Tran, Z. Bao, *Acc. Chem. Res.* 2018, 51, 1033.
- [16] Y. Lee, J. Park, A. Choe, S. Cho, J. Kim, H. Ko, *Adv. Funct. Mater.* 2019, 1904523.
- [17] C. Majidi, *Adv. Mater. Technol.* 2019, 4, 1800477.
- [18] G. Chen, N. Matsuhisa, Z. Y. Liu, D. P. Qi, P. Q. Cai, Y. Jiang, C. J. Wan, Y. J. Cui, W. R. Leow, Z. J. Liu, S. X. Gong, K. Q. Zhang, Y. Cheng, X. D. Chen, *Adv. Mater.* 2018, 30, 1800129.
- [19] T. H. Kim, C. S. Lee, S. Kim, J. Hur, S. Lee, K. W. Shin, Y. Z. Yoon, M. K. Choi, J. Yang, D. H. Kim, T. Hyeon, S. Park, S. Hwang, *ACS Nano* 2017, 11, 5992.
- [20] H. S. Liu, B. C. Pan, G. S. Liou, *Nanoscale* 2017, 9, 2633.
- [21] A. D. Valentine, T. A. Busbee, J. W. Boley, J. R. Raney, A. Chortos, A. Kotikian, J. D. Berrigan, M. F. Durstock, J. A. Lewis, *Adv. Mater.* 2017, 29, 1703817.
- [22] H. H. Shi, N. Khalili, T. Morrison, H. E. Naguib, *ACS Appl. Mater. Interfaces* 2018, 10, 19037.
- [23] N. Karim, S. Afroj, S. R. Tan, P. He, A. Fernando, C. Carr, K. S. Novoselov, *ACS Nano* 2017, 11, 12266.
- [24] C. Zhu, A. Chortos, Y. Wang, R. Pfattner, T. Lei, A. C. Hinckley, I. Pochorovski, X. Yan, J. W. F. To, J. Y. Oh, J. B. H. Tok, Z. Bao, B. Murmann, *Nat. Electron.* 2018, 1, 183.
- [25] M. Tavakoli, M. H. Malakooti, H. Paisana, Y. Ohm, D. G. Marques, P. A. Lopes, A. P. Piedade, A. T. de Almeida, C. Majidi, *Adv. Mater.* 2018, 30, 1801852.
- [26] H. Lee, M. Kim, I. Kim, H. Lee, *Adv. Mater.* 2016, 28, 4541.
- [27] P. C. Hsu, X. Liu, C. Liu, X. Xie, H. R. Lee, A. J. Welch, T. Zhao, Y. Cui, *Nano Lett.* 2015, 15, 365.
- [28] Y. J. Fan, X. Li, S. Y. Kuang, Y. Kuang, L. Zhang, Y. H. Chen, L. Liu, K. Zhang, S. W. Ma, F. Liang, T. Wu, Z. L. Wang, G. Zhu, *ACS Nano* 2018, 12, 9326.
- [29] Z. Jiang, M. O. G. Nayeem, K. Fukuda, S. Ding, H. Jin, T. Yokota, D. Inoue, D. Hashizume, T. Someya, *Adv. Mater.* 2019, 31, 1903446.
- [30] N. E. Persson, M. A. McBride, M. A. Grover, E. Reichmanis, *Chem. Mater.* 2017, 29, 3.
- [31] A. Philipp, N. W. Pech-May, B. A. F. Kopera, A. M. Lechner, S. Rosenfeldt, M. Retsch, *Anal. Chem.* 2019, 91, 8476.
- [32] H. M. Akram, M. Maqsood, H. Rashid, *Rev. Sci. Instrum.* 2009, 80, 075103.

# 03 Super-Resolution Microscopy by Movable Thin Films with Embedded Microspheres

Kenneth W. Allen, Navid Farahi, Yangcheng Li, Nicholas I. Limberopoulos, Dennis E. Walker Jr., Augustine M. Urbas, Vladimir Liberman, and Vasily N. Astratov

## ABSTRACT

Microsphere-assisted imaging has emerged as a simple technique to obtain optical super-resolution. This work addresses the methodology of the resolution measurements and the limited field-of-view provided by each sphere. It is suggested that a standard method of resolution analysis in far-field microscopy based on convolution with the point-spread function can be extended into the super-resolution area. This provides a unified approach to resolution measurements. To develop surface scanning functionality, high-index barium titanate glass microspheres were embedded in polydimethylsiloxane (PDMS) thin films. It is shown that such films adhere to nanoplasmonic structures' surface so that the tips of embedded spheres experience the objects' optical near-fields. Based on rigorous criteria, a resolution of approximately  $\lambda/6 - \lambda/7$  (where  $\lambda$  is the illumination wavelength) is demonstrated for arrays of gold (Au) dimers and bowties. Such films can be translated along the surface of investigated samples after liquid lubrication. It is shown that after lubrication, the resolution is diffraction-limited; however, the super-resolution gradually recovers as the lubricant evaporates. It is shown that such films adhere to nanoplasmonic structures' surface so that the tips of embedded spheres experience the objects' optical near-fields. Based on rigorous criteria, a resolution of approximately  $\lambda/6 - \lambda/7$  (where  $\lambda$  is the illumination wavelength) is demonstrated for arrays of gold (Au) dimers and bowties. Such films can be translated along the surface of investigated samples after liquid lubrication. It is shown that after lubrication, the resolution is diffraction-limited; however, the super-resolution gradually recovers as the lubricant evaporates.

## INTRODUCTION

Imaging by dielectric microspheres has emerged as a surprisingly simple way to obtain super-resolved images of nanoscale structures. [1–9] The method involves bringing a dielectric microsphere in contact with the investigated structure so that the microsphere experiences the object's optical near-field and creates a magnified virtual image that can be viewed by a standard microscope. Initially, the method has been demonstrated for micrometer-scale, low-index ( $n_s = 1.46$ ) silica spheres in air. [1] After that, this method was advanced by using high-index spheres ( $n_s > 1.8$ ) submerged in a liquid or embedded inside elastomeric slabs, [3] which improved the quality of images. [4, 8]

Based on a solid-immersion concept, the maximal diffraction-limited resolution available for high-index ( $n_s \sim 2.0$ ) barium titanate glass (BTG) microspheres can be estimated as  $\sim\lambda/4$ . Thus, the optical super-resolution by high-index spheres should be defined as a resolution better than  $\sim\lambda/4$ . One of the well-known approaches to experimentally measure super-resolution values is using "point" objects. [10] The image of an object is defined as a point-spread function (PSF) of the optical system. The PSF width represents the system's optical resolution. This concept is widely used in fluorescent (FL) microscopy, such as stimulated emission depletion (STED) [11] and other methods where bright "point" objects are readily available in the form of dye molecules or quantum dots.

To measure the resolution of microsphere-assisted imaging, researchers often select arrays containing features with recognizable shapes. [1–9] The basic idea of this approach is that the resolution of the optical system is equal to the characteristic dimensions of the minimum feature sizes that can be discerned. Different features have been studied by the microsphere-assisted technique that resulted in a broad range of resolution claims from  $\lambda/6$  to  $\lambda/17$ . [1, 4–7, 9]

In this work, we show that this approach can result in significantly overestimated resolution values. To solve this problem, we developed a resolution analysis based on a standard procedure of convolution with PSF, with subdiffraction-limited values allowed. A similar approach has been used previously to provide one-dimensional (1D) treatment with rectangular functions. [8] In the present work, we generalized this approach for 2D PSF and objects with arbitrary shape.

Furthermore, we developed a different approach to the field-of-view (FOV) limitations based on the incorporation of BTG spheres in polydimethylsiloxane (PDMS) thin films (or coverslips), as illustrated in **Figure 1**. The critical element of the coverslips' design is a planar array of high-index BTG microspheres with a broad range of diameters ( $2 < D < 53 \mu\text{m}$ ) held in the nanometer-scale proximity to the bottom surface of the coverslips. Once the coverslip is attached to a nanoplasmonic structure, the tips of microspheres can experience the object near-fields, leading to the possibility of super-resolution imaging. We show that the PDMS coverslips are naturally adherent to

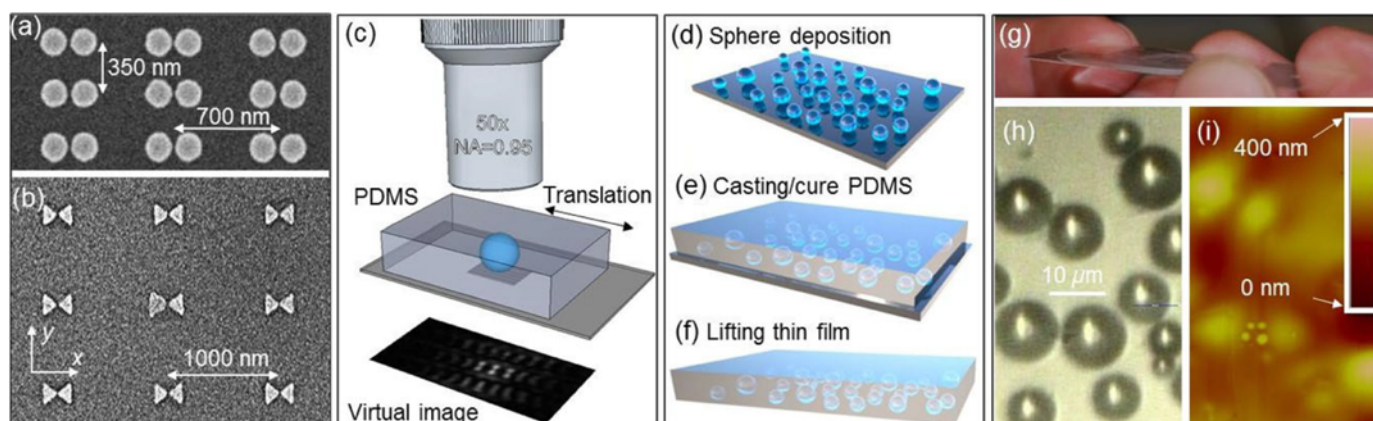


**Figure 1:** (a,b) SEM of the 2D arrays of golden dimers and bowties, respectively. (c) Schematic of the setup. (d–f) Step-by-step fabrication of coverslips with embedded spheres. (g) Photograph of the coverslips. (h) Microscopic image of the coverslip's bottom surface. (i) Mapping at the bottom surface by atomic force microscopy.

various substrates, providing imaging of Au dimers and bowties with  $\sim\lambda/6 - \lambda/7$  resolution. After surface lubrication with isopropyl alcohol (IPA), the coverslips can be translated along the surface. The ability to simultaneously capture images through the 2D array of spheres during wide-field microscopy allows precise alignment of microspheres with the objects of studies. We show that just after lubrication, the resolution is diffraction-limited. However, as the lubricant evaporates, the resolution gradually increases beyond the diffraction limit.

## METHODS

As objects for imaging, we used arrays of Au dimers and bowties illustrated by scanning electron microscopy (SEM) images in **Figure 1a** and **Figure 1b**, respectively.<sup>[8]</sup> The BTG spheres with larger barium (Ba) content have an index of  $n_s \sim 1.9$ , and the spheres with a larger titanium (Ti) content have an index of  $n_s \sim 2.1$  for the red portion of the visible region. Imaging was performed by an Olympus® LEXT™ OLS4000 scanning laser confocal microscope operating at  $\lambda = 405$  nm.

To fabricate the coverslips with embedded spheres, we used a three-step process<sup>[12]</sup> schematically illustrated in **Figure 1d-f**. This process bears some similarities with previously developed technology of embedding polystyrene microspheres in the PDMS membranes for applications in projection lithography.<sup>[13]</sup> First, the BTG spheres were deposited on the surface

of a microscope slide, where they formed a disordered monolayer. Then, a PDMS layer was cast over the spheres. It was cured at 90 °C (194 °F) for one hour. The photograph of this layer at the top of the microscope slide is presented in **Figure 1g**. Finally, this thin layer was lifted from the substrate with tweezers and used as a coverslip in super-resolution studies.

## RESULTS AND DISCUSSION

The microsphere-assisted imaging demonstrates significantly improved resolution. The virtual image of a dimer in **Figure 2a** obtained through the 5  $\mu\text{m}$  BTG sphere embedded in the PDMS coverslip is shown in **Figure 2b**. The virtual image of a bowtie in **Figure 2e** obtained through the embedded 53  $\mu\text{m}$  BTG sphere is shown in **Figure 2f**. Irradiance profiles along the x-axis of dimers and bowties are illustrated using red as color in **Figure 2d** and **Figure 2h**, respectively. The saddle-to-peak ratios of these profiles, 0.16 and 0.35, respectively, are significantly smaller than that assumed in various classical definitions of resolution of two-point sources<sup>[14,15]</sup>.

An attempt to define resolution based on the observation of minimal discernable features can lead to misleading results if, for example, we interpret the saddle point as a manifestation of a resolution of  $\sim 15$  nm gap in bowties, which would imply a resolution above  $\sim\lambda/27$ . As we show below, the image reconstruction with the Gaussian PSF

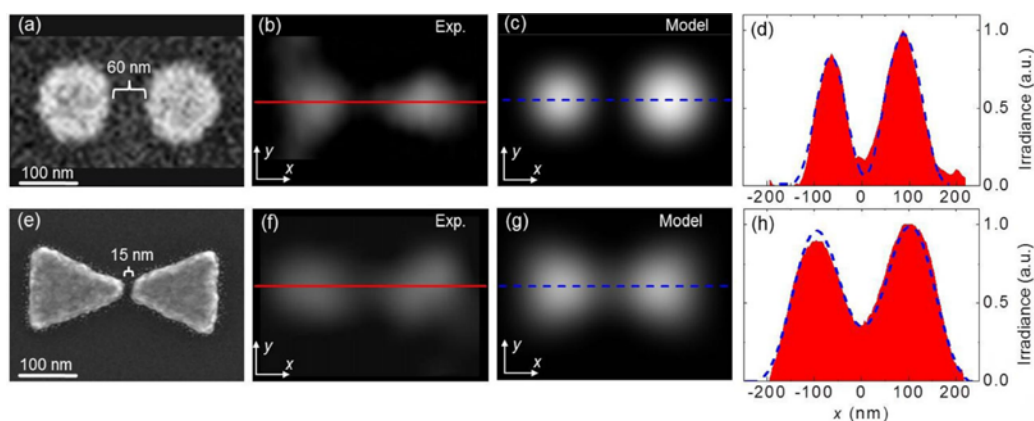


**Figure 2:** (a,e) SEM image of the Au dimer and bowtie, respectively. (b,f) Images of dimer and bowtie obtained through the 5  $\mu\text{m}$  and 53  $\mu\text{m}$  BTG microsphere, respectively. (c,g) Calculated convolutions of the idealized dimer and bowtie with the 2-D PSFs with FWHMs of  $\lambda/7$  and  $\lambda/5.5$ , respectively. (d,h) Comparison of the measured and calculated irradiance cross-sectional profiles.

with the width  $\sim\lambda/5.5$  allows obtaining a high-quality fit to the experimental results.

We treated the super-resolved images based on an analogy with the classical theory<sup>[16]</sup> where the image,  $I(x, y)$ , is considered as a convolution of a diffraction-limited PSF and the object's intensity distribution function,  $O(u, v)$ . This can be expressed in the standard integral form by **Equation 1**:

$$I(x, y) = \iint_{-\infty}^{\infty} O(u, v) \text{PSF}\left(u - \frac{x}{M}, v - \frac{y}{M}\right) du dv \quad (1)$$

in which the integration is performed in the object plane where the coordinates  $(x_0, y_0)$  are linearly related to the image plane via the magnification  $M$  as  $(x_0, y_0) = (x_i/M, y_i/M)$ . We used a Gaussian function for  $\text{PSF}(x_0, y_0)$  with the full width at half maximum (FWHM) being a fitting parameter. Based on the Houston criterion, fitted values of the FWHM in the object plane were considered a resolution of the system. To enable the super-resolution

analysis, we allowed subdiffraction-limited FWHM values; however, we kept the same basic **Equation 1** for image reconstruction.

Images calculated with 2D PSFs with FWHMs  $\sim\lambda/7$  and  $\sim\lambda/5.5$  are presented in **Figure 2c** and **Figure 2g** for dimers and bowties, respectively. An excellent agreement with experimental images was found. Blue dashed lines represent the calculated intensity profiles along the x-axis. They are also found to be in good agreement with the experiment.

To align embedded spheres with various objects, we developed a technique based on lubrication and locomotion of the entire PDMS thin film containing BTG spheres, as illustrated in **Figure 3**. The lubrication was provided by using IPA with  $n_s = 1.37$ . The locomotion of the coverslip was performed by a tapered stainless steel micro-probe inserted in the PDMS connected with a hydraulic micromanipulation controller, providing  $\sim 1 \mu\text{m}$  precision of the translation.

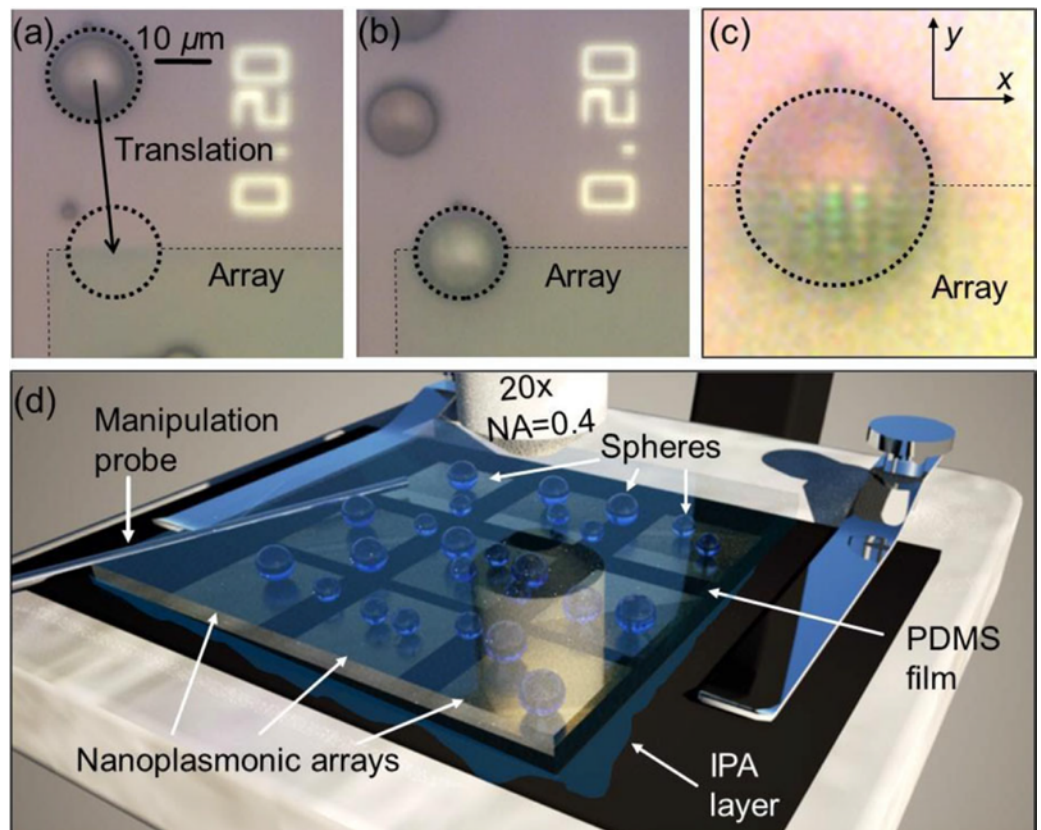


**Figure 3:** (a,b) Translation of the coverslip lubricated with IPA, and (c) the dimers are seen near the array's edge. (d) Experimental setup.

The translation and imaging through the coverslip immediately after its lubrication and application to the sample surface are illustrated in **Figure 3a-c**. Initially, the  $16\ \mu\text{m}$  BTG microsphere is located approximately  $40\ \mu\text{m}$  away from the border of the nanoplasmonic array (**Figure 3a**). As a result of the shift of the coverslip by  $\sim 40\ \mu\text{m}$ , this sphere is aligned with the edge of the array (**Figure 3b**). The virtual image of the array was obtained by the  $20\times$  ( $\text{NA} = 0.4$ ) objective lens by focusing deeper in the structure (**Figure 3c**). The diffraction-limited resolution of the microscope objective can be estimated as  $d = 0.515\lambda/\text{NA} \sim 700\ \text{nm}$ . However, experimentally, the  $700\ \text{nm}$  and  $350\ \text{nm}$  periods of the arrays can be discerned in the virtual image (**Figure 3c**). Immediately after lubrication, the internal structure of the dimers cannot be resolved.

Achieving super-resolution in such a situation requires reducing the thickness of the IPA layer due to its evaporation, as schematically illustrated in **Figure 4a**. Using geometrical optics, it can be shown that the lateral image magnification ( $M$ ) is related to the gap ( $g$ ) separating the spheres from the object by **Equation 2**:

$$M(n', r, g) = \frac{n'}{2(n' - 1)\left(\frac{g}{r} + 1\right) - n'} \quad (2)$$

where  $r$  is the radius of the sphere, and  $n' = n_{\text{sp}}/n_0 \sim 2.0/1.37 \approx 1.46$  is the refractive index contrast between the sphere and object space. The dependence of  $M$  on the normalized gap ( $g/r$ ) calculated using **Equation 2** is illustrated for  $n' = 1.5$  by the black line in **Figure 4b**. In the limit of  $g \ll r$ , **Equation 2** leads to  $|M| \sim |n'/(2-n')| \sim 3$ . The dynamical behavior of  $M$  as IPA evaporates was studied (**Fig-**

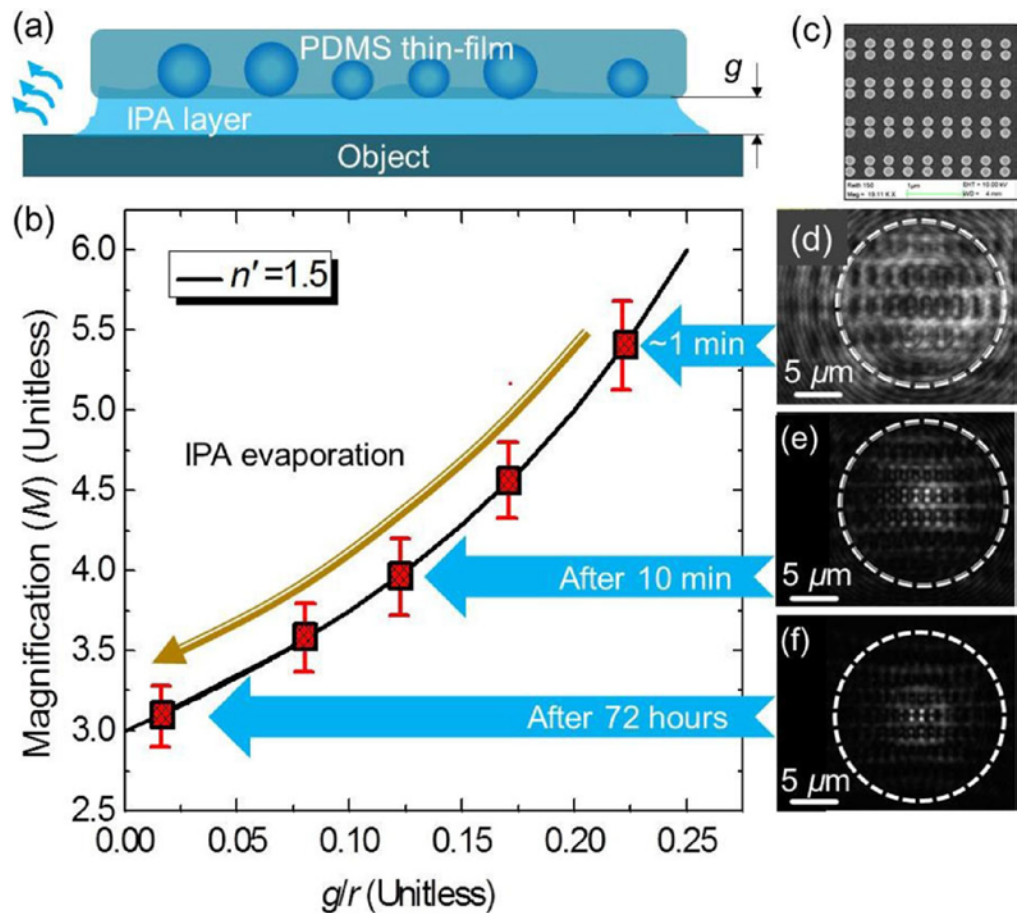


**Figure 4:** (a) Schematic illustration of the IPA layer evaporation. (b) Dynamical measurements of  $M$  (c) SEM image of the dimer array. Virtual images through the same sphere (d) after lubrication, (e) after 10 min, (f) after 72 hours.

Figure 4d-f). The magnification ( $M$ ) of the virtual image created by the  $16\ \mu\text{m}$  sphere embedded in a PDMS coverslip was determined using a comparison with the real image of the surface of the structure outside the microsphere<sup>[4]</sup>. The experimental results demonstrate a reduction of magnification from  $M \sim 5.4$  measured in the first minute (Figure 4d) to  $M \sim 3.1$  after 72 hours (Figure 4f).

The dimers were barely resolved within the first minute after lubrication and application of the coverslip (Figure 4d). However, the structure of individual dimers became much better visible in the images obtained later in the course of evaporation of the IPA layer, as seen in the magnified images after drying for 10 min and 72 hours (Figure 5a,c). Irradiance profiles along the x-axis of dimers are illustrated in Figure 5b and Figure 5d, respectively.

Using a PSF-based image fitting procedure described previously, we calculated intensity profiles along the x-axis, represented by

blue dashed lines. They demonstrate excellent agreement with the experimental intensity profiles at the FWHM of the Gaussian PSF fitting function at  $\sim\lambda/4$  and  $\sim\lambda/5.5$ . These results show that the super-resolution provided by the embedded BTG microspheres gradually increases as the IPA layer evaporates. The resolution values obtained after 72 hours ( $\sim\lambda/5.5$ ) almost reached the level of resolution obtained in structures without lubrication ( $\sim\lambda/6$ - $\lambda/7$ ).

## CONCLUSIONS

We showed that the observation of minimal discernible features in the optical images of extended objects (which cannot be approximated as point-sources) could result in overestimated resolution values. It is shown that a more consistent way of defining optical super-resolution is based on a standard procedure of convolution with PSF with widths smaller than the diffraction limit. We demon-

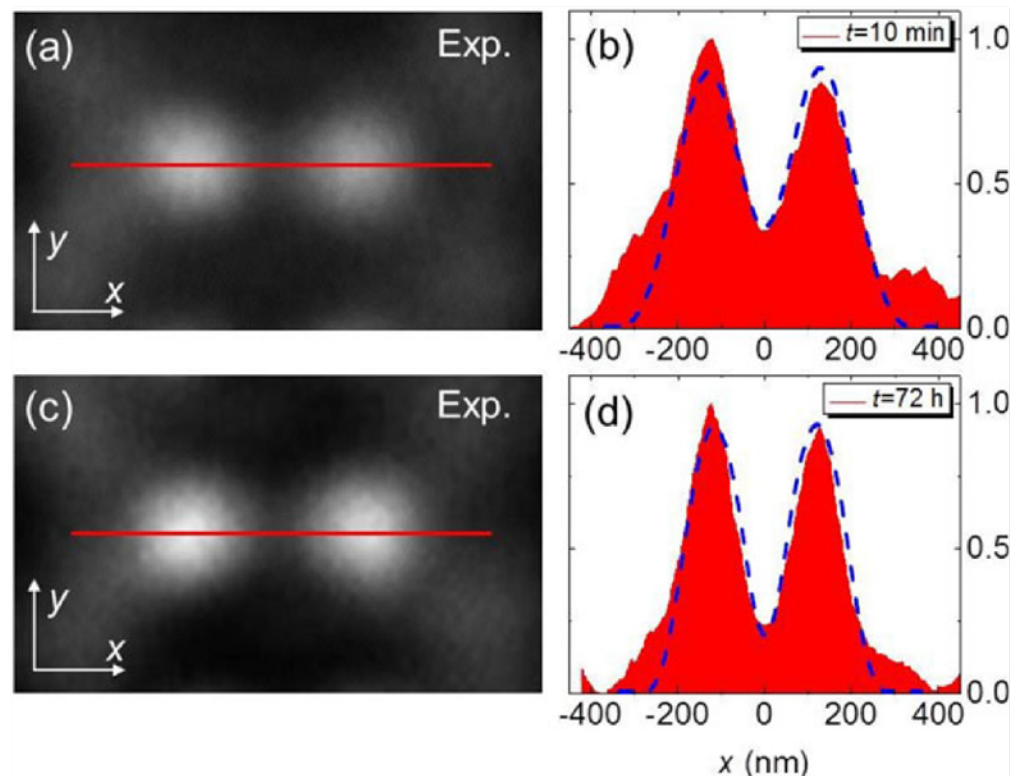


**Figure 5:** (a) Image of an Au dimer after 10 minutes of the IPA evaporation. (b) Comparison of the measured and calculated irradiance profiles. (c,d) Same as (a,b), respectively, but after drying for 72 hours.

strated that  $\sim\lambda/6$ – $\lambda/7$  resolution could be systematically achieved in the images of nanoscale metallic dimers and bowties. Another bottleneck problem of this technology is based on a limited FOV of virtual imaging through individual spheres. In this work, we developed a technology of fabrication of transparent elastomeric PDMS thin films containing hundreds of embedded high-index BTG microspheres. Such films or coverslips can be considered as a new optical component for super-resolution microscopy.

## REFERENCES

- [1] Z. Wang, W. Guo, L. Li, B. Luk'yanchuk, A. Khan, Z. Liu, Z. Chen, and M. Hong, *Nat. Commun.* 2011, 2, 218.
- [2] X. Hao, C. Kuang, X. Liu, H. Zhang, and Y. Li, *Appl. Phys. Lett.* 2011, 99, 203102.
- [3] V.N. Astratov, and A. Darafsheh. "Methods and systems for super-resolution optical imaging using high-index of refraction microspheres and microcylinders." U.S. Patent No. 9,726,874. 8 Aug. 2017.
- [4] A. Darafsheh, G. F. Walsh, L. Dal Negro, and V. N. Astratov, *Appl. Phys. Lett.* 2012, 101, 141128.
- [5] L. Li, W. Guo, Y. Yan, S. Lee, and T. Wang, *Light: Science & Applications* 2013, 2, e104.
- [6] L. A. Krivitsky, J. J. Wang, Z. Wang, and B. Luk'yanchuk, *Sci. Reports* 2013, 3, 3501.
- [7] H. Yang, N. Moullan, J. Auwerx, and M. A. M. Gijs, *Small* 2014, 10, 1712–1718.
- [8] A. Darafsheh, N.I. Limberopoulos, J.S. Derov, D. E. Walker, Jr., and V. N. Astratov, *Appl. Phys. Lett.* 2014, 104, 061117.
- [9] Y. Yan, L. Li, C. Feng, W. Guo, S. Lee, and M. Hong, *ACS Nano* 2014, 8, 1809–1816.
- [10] S. Weisenburger and V. Sandoghdar, *Contemporary Physics* 2015, 56, 123–143.
- [11] G. Donnert, J. Keller, R. Medda, M. A. Andrei, S. O. Rizzoli, R. Luhrmann, R. Jahn, C. Eggeling, and S.W. Hell, *Proc. Natl. Acad. Sci. USA* 2006, 03, 11440–11445.
- [12] E. C. H. Sykes, S. P. Ashili, A. V. Kanaev, and V. N. Astratov, in *IEEE Proceedings of OSA Topical Meeting on Informational Photonics, Charlotte, NC, 6-8 June 2005*, paper No. IThD3.
- [13] M.-H. Wu and G.M. Whitesides, *Appl. Phys. Lett.* 2000, 78, 2273–2280.
- [14] A. Lipson, S. G. Lipson, and H. Lipson, *Optical Physics*, 4th Ed., (Cambridge University Press, New York, 2011).
- [15] A. J. den Dekker and A. van den Bos, *J. Opt. Soc. Am. A* 1997, 14, 547–557.
- [16] J. W. Goodman, *Introduction to Fourier Optics*, 2nd Ed., (The McGraw-Hill Companies, New York, 1996).

# 04 Flexible Micropillar Electrode Arrays for In Vivo Neural Activity Recordings

Mingde Du, Shouliang Guan, Lei Gao, Suye Lv, Siting Yang, Jidong Shi, Jinfen Wang, Hongbian Li, and Ying Fang

## ABSTRACT

Flexible electronics that can form tight interfaces with neural tissues hold great promise for improving the diagnosis and treatment of neurological disorders and advancing brain/machine interfaces. Here, the facile fabrication of a novel flexible micropillar electrode array ( $\mu$ PEA) is described based on a biotemplate method. The flexible and compliant  $\mu$ PEA can readily integrate with the soft surface of a rat cerebral cortex. Moreover, the recording sites of the  $\mu$ PEA consist of protruding micropillars with a nanoscale surface roughness that ensures tight interfacing and efficient electrical coupling with the nervous system. As a result, the flexible  $\mu$ PEA allows for in vivo multichannel recordings of epileptiform activity with a high signal-to-noise ratio. The ease of preparation and high flexibility make the  $\mu$ PEA an attractive tool for in vivo spatiotemporal mapping of neural activity.

## INTRODUCTION:

Neural electrodes can be used to develop an understanding of brain functions and have become a clinical tool for the diagnosis and treatment of neurological disorders. [1-8] In particular, epilepsy is a common neurological disorder that affects about 1% of the general population and 4% of children. [9] Clinically, about 30% of patients with epilepsy respond poorly to antiepileptic drugs and have to undergo surgical resection of the epileptic foci. Subdual intraoperative electrocorticography (ECoG) has been routinely applied in patients with intractable epilepsy for both preoperative localiza-

tion of the epileptogenic focus and assessment of post-surgical outcomes. [10-12] ECoG recordings are typically performed with subdual electrode arrays that are placed directly on a cerebral cortex's surface. [13] Subdual electrodes are much less invasive than penetrating depth electrodes that cause tissue damage and elicit a pronounced foreign body response. [14,15]

The interfaces between electrodes and neural tissues play an essential role in recording neural activity because extracellular signals decay rapidly with distance. [16,17] A key challenge for creating tight interfaces between conventional subdual electrodes and neural tissues has been their sizeable mechani-

cal mismatch. [18] The poor contacts between conventional rigid electrodes and soft tissues lead to the poor electrical coupling at their interfaces. As a result, neural activity signals can be notably attenuated by the cerebrospinal fluid in the electrode-tissue gaps. [19]

Flexible subdural electrodes based on polymer substrates have been developed to improve the contacts between electrodes and neural tissues. [20-25] In addition, they were shown to reduce the foreign body response of the brain tissue in chronic applications. [26] Nevertheless, the moduli of the polymer substrates are in MPa to GPa range, [27] which is still orders of magnitude higher than that of the brain. This can cause shear force and micromotion at the electrode-tissue interfaces, limiting the accuracy and stability of subdural ECoG recordings.

Here, we introduce a flexible subdural micropillar electrode array ( $\mu$ PEA) that enables the formation of tight neural interfaces and stable neural activity recordings. The recording sites of the  $\mu$ PEA consist of protruding microscale pillars with nanoscale roughness obtained by replicating the surface of a lotus leaf. The hierarchical surface structure affords lower impedance compared to planar electrodes. In addition, the protruding micropil-

lars create a tight interface and effective electrical coupling between the electrodes and the cerebral cortex of a rat brain. As a result, the  $\mu$ PEAs have been successfully demonstrated for stable multichannel recordings of epileptiform activity with high SNR of  $252 \pm 35$ .

## METHODS

The fabrication process of a  $\mu$ PEA is illustrated in **Figure 1**. PDMS base was mixed with a curing agent and poured onto a lotus leaf and cured at 50 °C (122 °F) for 1 hour. After peeling off the lotus leaf, a PDMS negative template was obtained. The template was treated with oxygen plasma at 100 W for 5 minutes. Then, a polyimide (PI) mask with a 3 × 3 hole array was transferred onto the PDMS template. The PI mask/PDMS was heated at 140 °C (284 °F) for 30 minutes under a pressure of  $\approx 20$  kPa to increase their adhesion. A PI precursor solution was then spin-coated onto the PI mask/PDMS. The system was heated at 120 °C (248 °F) for 20 minutes for the removal of the solvent and then 200 °C (392 °F) for 30 minutes in a vacuum for curing. After peeling off the PDMS template, a PI substrate with spatially patterned micro-

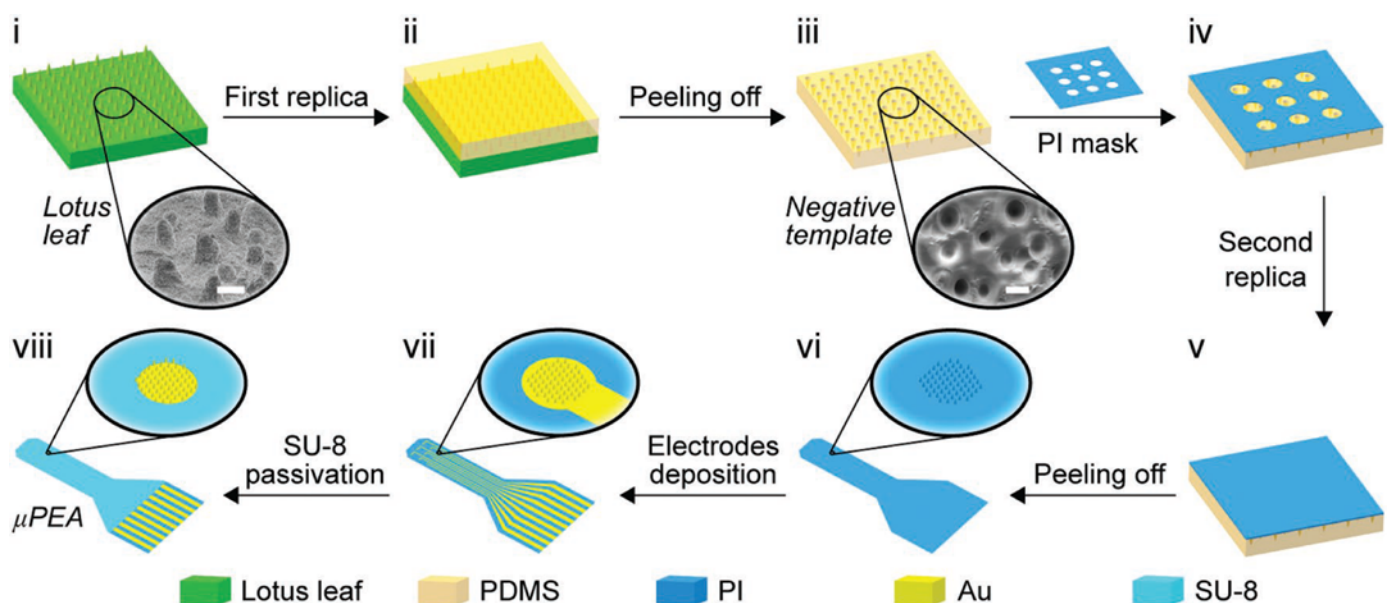


**Figure 1:** i) A flat lotus leaf, inset shows SEM image; ii) PDMS was poured on the surface of lotus leaf and cured; iii) PDMS negative template with random distributed microcavities, inset shows SEM image of a PDMS negative template; iv) PDMS negative template covered with PI mask; v) PI was spin-coated on the template and cured; vi) PI substrate with spatially patterned hierarchical micro-pillars; (vii, viii)  $\mu$ PEA before and after SU-8 passivation. Scale bars: 10  $\mu$ m.

pillars was obtained. Planar electrode arrays (PEAs) were also fabricated for comparison.

Neural electrode arrays were defined on a patterned PI substrate by thermal deposition of chromium/gold (Cr/Au) (10 nm/200 nm). The recording sites were aligned with the patterned micropillar regions of the PI substrate. Then a SU-8 passivation layer was defined by photolithography to encapsulate the planar interconnect lines. The  $\mu$ PEA was bonded to a flexible flat cable through anisotropic conductive film.

3D confocal images of the micropillar electrodes were acquired on a laser confocal microscope (Olympus® LEXT™ OLS4000 system).

Scanning electron microscopy (SEM) images were collected using a FEI Nova NanoSEM 430 system and Hitachi-SU8220. Cross-sections of the electrodes were obtained by focused ion beam (FIB) etching using a FIB/SEM dual-beam system. Electrochemical impedance spectroscopy (EIS) of the electrodes was measured using an electrochemical workstation (Reference 3000, Gamry Instruments). A Platinum (Pt) rod and an Ag/AgCl electrode (CHI111, CH Instruments) were used as counter and reference electrodes, respectively.

A Sprague-Dawley rat was anesthetized and fixed in a stereotaxic apparatus. Craniotomy was performed, and the left hemisphere

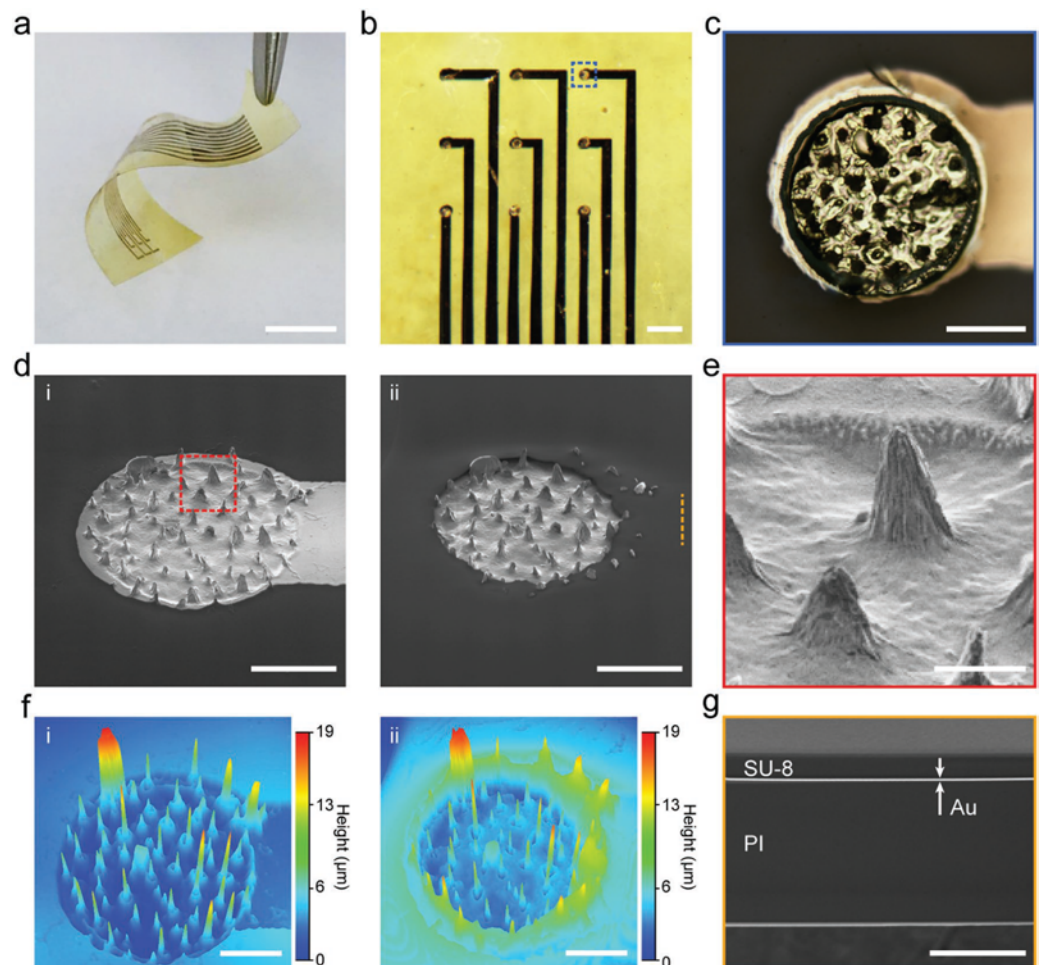


**Figure 2:** Structure of flexible  $\mu$ PEA. a) A flexible  $\mu$ PEA. Scale bar: 5 mm. b) Optical image of the  $3 \times 3$  micropillar electrode array. Scale bar: 500  $\mu\text{m}$ . c) Optical image of the recording site marked with dashed blue box in inset (b). Scale bar: 50  $\mu\text{m}$ . d) SEM image of an electrode (i) before and (ii) after passivation. Scale bars: 50  $\mu\text{m}$ . e) Magnified SEM image of the area marked with dashed red box in insets (d-(i)). Scale bar: 10  $\mu\text{m}$ . f) 3D confocal images of the electrode in inset (d-(i)) before and (d-(ii)) after passivation. Scale bars: 50  $\mu\text{m}$ . g) Cross-sectional SEM image of the interconnect line marked with dashed orange line in inset (d-(ii)). Scale bar: 10  $\mu\text{m}$ .

was exposed, and the dura mater was carefully removed. A flexible  $\mu$ PEA was placed on the exposed subdural surface of the rat cortex. The neural signals were recorded at a sampling rate of 1 kHz.

## RESULTS AND DISCUSSION

**Figure 2a** shows an as-prepared  $\mu$ PEA with a final thickness of 18  $\mu\text{m}$ . The  $\mu$ PEA is highly flexible and can be bent repeatedly without loss of structural integrity. The  $\mu$ PEA consists of nine recording sites arranged in  $3 \times 3$  matrices with 1 mm spacing (**Figure 2b**). Each recording site has a diameter of 120  $\mu\text{m}$  (**Figure 2c**). SEM images of a typical electrode before and after SU-8 passivation are shown in **Figure 2d**. The enlarged SEM images in **Figure 2e** show that the micropillars contain nanoscale wrinkles. The height of the wrinkles ranges from 100 nm – 200 nm. 3D confocal images show that the  $\mu$ PEA consists of protruding micropillars (**Figure 2f**). **Figure 2g** shows a cross-sectional SEM image of a planar interconnects line, which consists of a three-layer sandwich structure of SU-8/Au/PI.

The performance of neural electrodes is mainly limited by the thermal noise that arises from the impedance at the electrode-electrolyte interface.<sup>[28]</sup> The impedance at the electrode-electrolyte interface is inversely proportional to the effective electrode area. We performed electrochemical impedance spectroscopy (EIS) on micropillar and planar elec-

trodes on the same PI substrate for direct comparison. **Figure 3a** shows representative EIS results measured in phosphate-buffered saline (PBS). The impedance of the micropillar electrode is lower than the planar one. The reduced impedance can be attributed to the increased electrode area. **Figure 3b** summarizes the averaged impedance of 6 micropillar electrodes and 27 planar electrodes measured at 1 kHz.

We applied the  $\mu$ PEAs for in vivo subdural recordings of penicillin-induced epileptiform activity in the rat cortex. As an antagonist of the gamma-aminobutyric acid (GABA) receptor, penicillin induces epileptiform activity by preventing GABA-mediated inhibitory control of pyramidal neurons.<sup>[29]</sup> As shown in **Figure 4a**, the  $\mu$ PEA conformally covered a large cortical area of the rat brain. Notably, the protruding micropillars at the recording sites were engulfed by the neural tissue, which resulted in significantly improved electrical coupling.

**Figure 4b** shows a representative real-time signal recorded by a micropillar electrode (Ch-9), and **Figure 4c** is the normalized time-frequency spectral analysis of the time-series data. As shown in **Figure 4d**, three periods, including the basal period, latent period, and epileptiform activity period, could be identified. The epileptiform activity period began with increasing discharges arising from the hyperexcitability and hypersynchrony of neuronal activity. As shown in **Figure 4c**, there was an associated increase in the spectral power between 5 Hz – 25 Hz. The amplitude of the discharges reached a maximum of 3.5 mV at 0.5 h after penicillin injection, and the  $\mu$ PEA

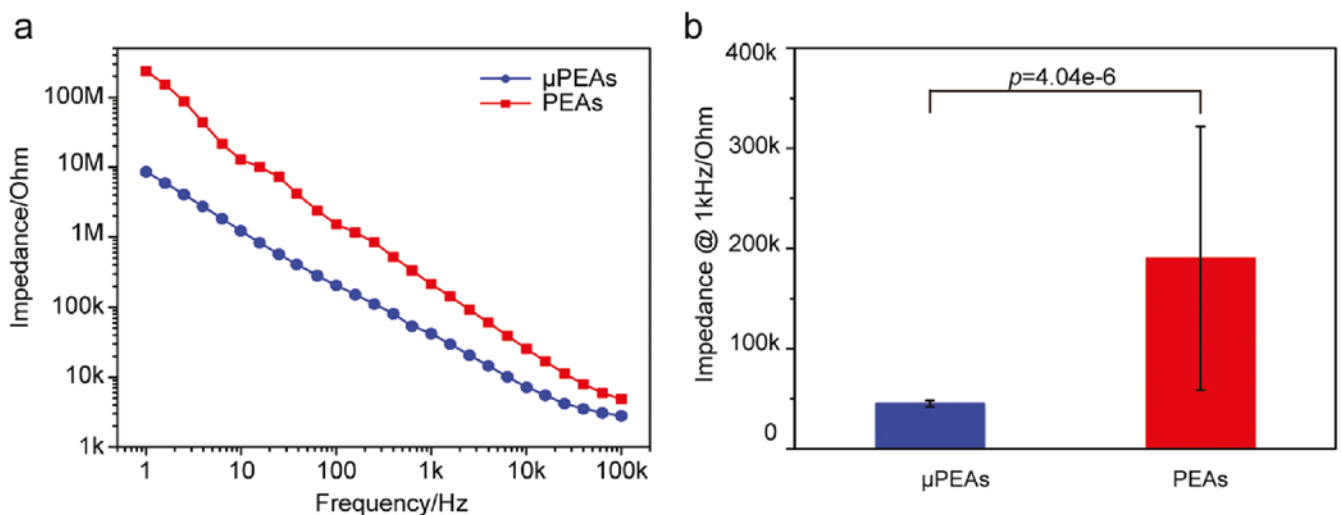


**Figure 3:** a) EIS of micropillar and planar electrodes measured in PBS. b) Averaged impedance of micropillar and planar electrodes

allowed stable recordings over 3 h. The discharge frequency decreased from 0.8 spikes/s in the initial period to 0.2 spikes/s in the late epilepsy period. The high signal amplitude could be attributed to the tight interfaces and efficient electrical coupling between the protruding micropillars and neural tissue.

**Figure 4e,f** shows simultaneous multichannel recordings by the  $\mu$ PEA. We applied a thresholding method to detect epileptiform discharges recorded by the nine channels, from which spike times were extracted (**Figure 4g**). Spike-time delays at different channel locations were then calculated relative to the spike-time

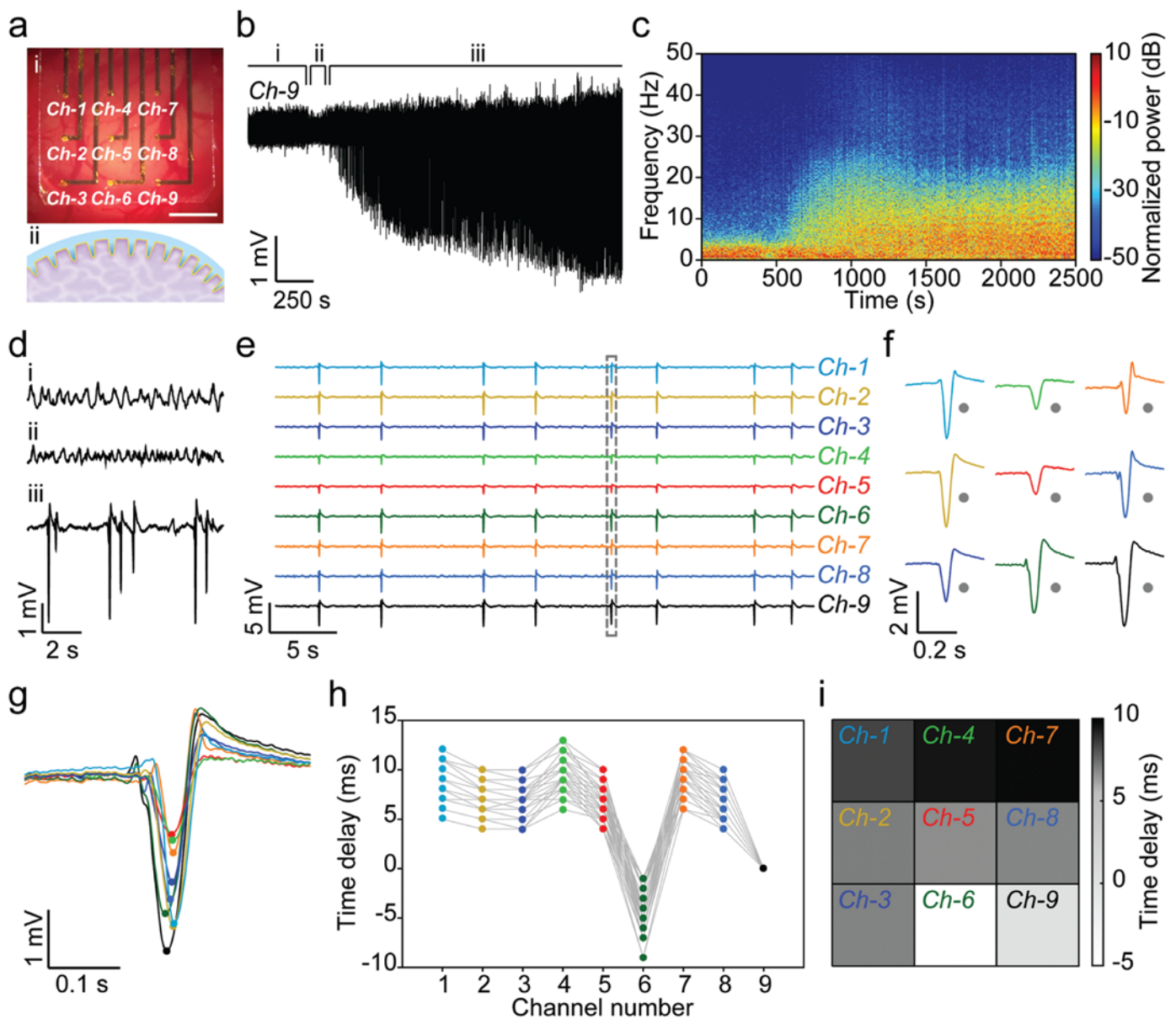


**Figure 4:** In vivo neural activity recordings with  $\mu$ PEA. a-(i) Optical image of a  $\mu$ PEA conformally attached onto the cortical surface of rat brain and a-(ii) schematic illustration of the tight interface between micropillars and brain tissue. Scale bar in (i): 1 mm. b) Representative real-time recording of neural activity by a micropillar electrode (Ch-9). c) Normalized time-frequency spectrum of the time-series data in inset (b). d-(i) Neural signals recorded during the basal period, d-(ii) latent period, and d-(iii) epileptiform activity period, respectively. e) Multi-channel recordings of epileptiform activity with the  $\mu$ PEA. f) Array layout of the voltage traces during an epileptiform discharge, as marked with the dashed black box in inset (e). g) Overlaid voltage traces. The colored dots marked the spike-times. h) Spike-time delays of 50 discharges recorded by the nine channels in a 255-s window. i) Array layout of the average spike-time delays determined from inset (h).

of Ch-9. **Figure 4h** summarized the spike-time delays of 50 epileptiform discharges recorded in a 255 s window. The spike-time delays show a clear dependence on the channel locations. This allowed us to construct a pattern map by plotting the average spike-time delays as a function of each channel's location (**Figure 4i**).

## CONCLUSIONS

In summary, we demonstrated a facile bio-template method for the fabrication of flexible  $\mu$ PEAs. The hierarchical surface structure of the  $\mu$ PEAs effectively reduced the impedance of the micropillar electrodes. Moreover, a tight electrode-neural interface was obtained due to the engulfment of the micropillars by neural tissues. As a result, the  $\mu$ PEAs allowed stable subdural recordings of neural activity with high SNR. Multichannel recordings further revealed the propagation characteristics of epileptiform activity across the cerebral cortex. These results show that flexible  $\mu$ PEAs can offer new opportunities to study the tempo-spatial dynamics of neural activities.

## REFERENCES

- [1] P. K. Campbell, K. E. Jones, R. J. Huber, K. W. Horch, R. A. Normann, *IEEE Trans. Biomed. Eng.* 1991, 38, 758.
- [2] J. L. Collinger, B. Wodlinger, J. E. Downey, W. Wang, E. C. Tyler-Kabara, D. J. Weber, A. J. C. McMorland, M. Velliste, M. L. Boninger, A. B. Schwartz, *Lancet* 2013, 381, 557.
- [3] A. K. Engel, C. K. E. Moll, I. Fried, G. A. Ojemann, *Nat. Rev. Neurosci.* 2005, 6, 35.
- [4] R. S. Fisher, A. L. Velasco, *Nat. Rev. Neurol.* 2014, 10, 261.
- [5] C. M. Gray, P. E. Maldonado, M. Wilson, B. McNaughton, *J. Neurosci. Methods* 1995, 63, 43.
- [6] G. Hong, R. D. Viveros, T. J. Zwiang, X. Yang, C. M. Lieber, *Biochemistry* 2018, 57, 3995.
- [7] J. J. Jun, N. A. Steinmetz, J. H. Siegle, D. J. Denman, M. Bauza, B. Barbarits, A. K. Lee, C. A. Anastassiou, A. Andrei, Ç. Aydın, M. Barbic, T. J. Blanche, V. Bonin, J. Couto, B. Dutta, S. L. Gratiy, D. A. Gutnisky, M. Häusser, B. Karsh, P. Ledochowitsch, C. M. Lopez, C. Mitelut, S. Musa, M. Okun, M. Pachitariu, J. Putzeys, P. D. Rich, C. Rossant, W.-I. Sun, K. Svoboda, M. Carandini, K. D. Harris, C. Koch, J. O'Keefe, T. D. Harris, *Nature* 2017, 551, 232.
- [8] J. S. Perlmutter, J. W. Mink, *Annu. Rev. Neurosci.* 2006, 29, 229.
- [9] A. T. Berg, C. P. Panayiotopoulos, *Neurology* 2000, 55, 1073.
- [10] P. Jayakar, M. Duchowny, T. J. Resnick, *J. Child Neurol.* 1994, 9, 2S61.
- [11] K. Lehnertz, C. E. Elger, *Electroencephalogr. Clin. Neurophysiol.* 1995, 95, 108.
- [12] M. J. Morrell, *Neurology* 2011, 77, 1295.
- [13] W. J. Freeman, L. J. Rogers, M. D. Holmes, D. L. Silbergeld, *J. Neurosci. Methods* 2000, 95, 111.
- [14] R. Biran, D. C. Martin, P. A. Tresco, *Exp. Neurol.* 2005, 195, 115.
- [15] P. J. Rousche, R. A. Normann, *J. Neurosci. Methods* 1998, 82, 1.
- [16] G. H. Kim, K. Kim, E. Lee, T. An, W. Choi, G. Lim, J. H. Shin, *Materials* 2018, 11, 1995.
- [17] E. W. Schomburg, C. A. Anastassiou, G. Buzsáki, C. Koch, *J. Neurosci.* 2012, 32, 11798.
- [18] C. K. Im, J. M. Seo, *Biomed. Eng. Lett.* 2016, 6, 104.
- [19] G. Buzsáki, C. A. Anastassiou, C. Koch, *Nat. Rev. Neurosci.* 2012, 13, 407.
- [20] D. Khodagholy, T. Doublet, M. Gurfinkel, P. Quilichini, E. Ismailova, P. Leleux, T. Herve, S. Sanaur, C. Bernard, G. G. Malliaras, *Adv. Mater.* 2011, 23, H268.
- [21] D. Khodagholy, J. N. Gelinias, T. Thesen, W. Doyle, O. Devinsky, G. G. Malliaras, G. Buzsaki, *Nat. Neurosci.* 2015, 18, 310.
- [22] J.-H. Kim, G. Kang, Y. Nam, Y.-K. Choi, *Nanotechnology* 2010, 21, 085303.
- [23] J. Viventi, D.-H. Kim, L. Vigeland, E. S. Frechette, J. A. Blanco, Y.-S. Kim, A. E. Avrin, V. R. Tiruvadi, S. W. Hwang, A. C. Vanleer, D. F. Wulsin, K. Davis, C. E. Gelber, L. Palmer, J. Van der Spiegel, J. Wu, J. Xiao, Y. Huang, D. Contreras, J. A. Rogers, B. Litt, *Nat. Neurosci.* 2011, 14, 1599.
- [24] I. R. Mineev, P. Musienko, A. Hirsch, Q. Barraud, N. Wenger, E. M. Moraud, J. Gandar, M. Capogrosso, T. Milekovic, L. Asboth, R. F. Torres, N. Vachicouras, Q. H. Liu, N. Pavlova, S. Duis, A. Larmagnac, J. Vörös, S. Micera, Z. G. Suo, G. Courtine, S. P. Lacour, *Science* 2015, 347, 159.
- [25] Y. Guo, Z. Fang, M. Du, L. Yang, L. Shao, X. Zhang, L. Li, J. Shi, J. Tao, J. Wang, H. Li, Y. Fang, *Nano Res.* 2018, 11, 5604.
- [26] J. W. Jeong, G. Shin, S. I. Park, K. J. Yu, L. Xu, J. A. Rogers, *Neuron* 2015, 86, 175.
- [27] J. P. Seymour, F. Wu, K. D. Wise, E. Yoon, *Microsyst. Nanoeng.* 2017, 3, 16066.
- [28] E. Huigen, A. Peper, C. A. Grimbergen, *Med. Biol. Eng. Comput.* 2002, 40, 332.
- [29] R. L. Macdonald, J. L. Barker, *Nature* 1977, 267, 720.

Copyright:

DOI: 10.1002/sml.201900582;  
M. Du, S. Guan, L. Gao, S.  
Lv, S. Yang, J. Shi, J. Wang,  
H. Li, and Y. Fang;  
small;

© 2019 WILEY-VCH Verlag  
GmbH & Co. KGaA, Weinheim

# Scientific Publishing

**TWO OF THE MOST IMPORTANT PARTS** of a scientific article are their title and the abstract. They are the first opportunity to attract the attention of the editor, reviewer or reader and play into search engine optimization (SEO) of your article. Herein, you can find a detailed description that will guide you through the creation of a concise title and a well-structure abstract.

# 5 tips for writing better science papers

1

Don't underestimate the importance of your cover letter

A good cover letter explains to the editor the critical question your research addresses, how you have answered this question, and why it is of significance to the wider community.



2

Keep the title simple: be consistent, not too technical, and concise

It's important to grab the attention of your editor/reviewer/reader right away and give them an idea of why your paper is a scientific breakthrough. The title also plays into search engine optimization for your article, so think of which search terms you would use when searching for your paper, and try to incorporate those keywords into your title.





4

## Introduce your research with its importance

The reader needs to know the background to your research and, most importantly, why your research is important in this context. What critical questions does your research address? Why should the reader be interested?

3

## Don't cram the abstract with details

What you want is to grab the reader's attention with the first statement, add a few of the most important details, then leave them with the overall message of the manuscript in the last sentence.



5

## You might be tempted to share all your war stories... but don't

When reporting results, keep your focus and make your R&D concise but informative.



# Scientific Publishing: Title and Abstract

P. Trevorrow, G. E. Martin

This article is a short version of the comprehensive and freely available tutorial "How to write a research article for MRC", written by Paul Trevorrow and Gary E. Martin.

## ARTICLE TITLE

When choosing a title for an article, it is advisable to choose a title that best describes the work, is succinct, and free from excessive jargon. The title should entice the reader and authors should keep in mind that the first impression counts! A strong title will likely convince an editor (or reviewer) that the paper is important to the journal's readership. Titles should generally be short, not more than 15 words, and be informative; they need to convey the main message and/or finding of the paper. Try to be precise without using vague language. It is recommended that authors of research articles and reviews avoid titles such as the following:

- "Studies on ...".
- "Characterization of ...".
- "Optimization of ...".
- "Investigations on ...".
- "Review of ...".
- "... in review".

In some publications, references to "new" or "novel" appear frequently in article titles. Such phrases should be avoided where possible. The point of the academic journal is to publish new research so stating new or novel in the title can appear somewhat redundant.

## THE ABSTRACT

Your abstract is one of the most important elements of your article. Firstly, editors may not have time to read your entire manuscript when making initial screening decisions. If you can sell them on the importance of your research in the abstract, they will be able to make a decision on whether the article is acceptably within the scope of the journal quickly and

easily. Secondly, when asked to review an article, referees are presented with the abstract in the initial invitation. A poorly structured abstract with unclear motivation is less likely to be accepted for review by an already fatigued referee. Finally, due to abstracting and indexing agencies, such as Web of Science, SciFinder, PubMed, ResearchGate (the list goes on), more people are going to view your abstract than will ever read your paper. If you can make it clear why your article is important, it is more likely to be discovered by the correct audience.

The abstract should be viewed as a self-contained component and should not include references to external sources or supporting information. The abstract should also be concise so that editors, reviewers, or the eventual readers can quickly make an assessment on whether they want to read the full paper.

One should think of an abstract in sections, firstly state the problem, the reason for the research, and why it is important. Remember that your abstract is the biggest advert for your paper, so it is important to put the research in a broad context stating why the research is important to a broad public audience and not only your specialist NMR community. Secondly, introduce the procedure simply, describing the investigative technique and the samples involved. Thirdly, offer a brief and succinct account of the result followed by the final portion, the conclusion. The conclusion should convey the take-home message of the research. In general, an optimal abstract should follow the following structure, which will ensure that all of the important points are covered and expressed logically:

- **Rationale:** state the problem, the reason for the research and why it is important to broad non-specialist audience.
- **Method:** what procedure/analysis has been undertaken?

- **Result:** what was the outcome of the experiment?
- **Conclusion:** what are the key take-home messages of the research?

---

## EXAMPLE

All articles in this eBook give examples of well-structured abstracts. For example, the abstract of “Flexible Micropillar Electrode Arrays for In Vivo Neural Activity Recordings” (pp. 25-31) mimics the above mentioned, recommended structure:

- **Rationale**  
“Flexible electronics that can form tight interfaces with neural tissues hold great promise for improving the diagnosis and treatment of neurological disorders and advancing brain/machine interfaces.”
- **Method**  
“Here, the facile fabrication of a novel flexible micropillar electrode array ( $\mu$ PEA) is described based on a biotemplate method.”

- **Result**  
“The flexible and compliant  $\mu$ PEA can readily integrate with the soft surface of a rat cerebral cortex. Moreover, the recording sites of the  $\mu$ PEA consist of protruding micropillars with a nanoscale surface roughness that ensures tight interfacing and efficient electrical coupling with the nervous system. As a result, the flexible  $\mu$ PEA allows for in vivo multichannel recordings of epileptiform activity with a high signal-to-noise ratio.”
  - **Conclusion**  
The ease of preparation and high flexibility make the  $\mu$ PEA an attractive tool for in vivo spatiotemporal mapping of neural activity.”
- 

When reading an article, the abstract appears as the first element; however, it may be prudent to compose this last when writing up the manuscript. This will enable one to keep consistent with the findings of the research and prevent rewriting as the investigative components of the article develop.